

First Principles Reaction Discovery: From the Schrodinger Equation to Experimental Prediction for Methane Pyrolysis

Rui Xu,^{1,2} Jan Meisner,^{1,2,a} Alexander M. Chang,^{1,2} Keiran C. Thompson,^{1,2}
and Todd J. Martínez^{1,2,*}

¹Department of Chemistry and The PULSE Institute, Stanford University, Stanford, CA 94305

²SLAC National Accelerator Laboratory, 2575 Sand Hill Road, Menlo Park, CA 94025

*Corresponding author: toddjmartinez@gmail.com

^aPresent address: Institute for Physical Chemistry, Heinrich Heine University, Düsseldorf, 40225, Germany

Table of contents:

Section S1. Species List in the Nanoreactor Kinetic Model.	S2
Section S2. Information about Literature Kinetic Models	S5
Section S3. Reaction Discovery Runs and an Example of Temperature Plot.	S6
Section S4. Charge and Spin Multiplicity Assignment for Species and Reactions.	S7
Section S5. Thermochemistry Calculations.	S9
Section S6. Reaction Rate Parameter Calculations.	S19
Section S7. Additional Details in Kinetic Modeling.	S23
Section S8. Examples of “Rare Events” During Reaction Discovery Runs.	S26
Section S9. Discussion on Chemically Activated Reaction $2\text{CH}_3 \leftrightarrow \text{C}_2\text{H}_5 + \text{H}$.	S28
Section S10. Additional Results from the Sensitivity Analysis.	S31
References	S35

Figures:

Figure S1	S6
Figure S2	S13
Figure S3	S18
Figure S4	S21
Figure S5	S25
Figure S6	S26
Figure S7	S29
Figure S8	S29
Figure S9	S30
Figure S10	S31
Figure S11	S31
Figure S12	S32
Figure S13	S32
Figure S14	S33
Figure S15	S34

Tables:

Table S1	S2
Table S2	S5
Table S3	S7
Table S4	S14
Table S5	S18
Table S6	S22
Table S7	S23
Table S8	S24
Table S9	S27
Table S10	S29



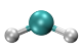

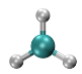
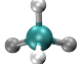
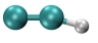
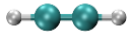
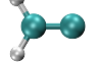
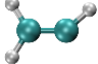
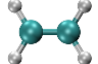
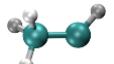
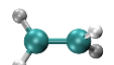
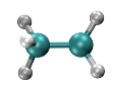
Additional attachment:

Cantera model file:
nr_ch4_pyrolysis.cti

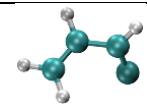
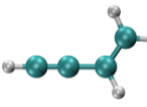
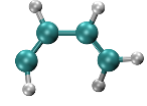
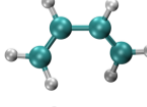
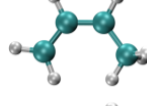
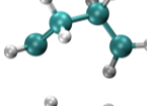
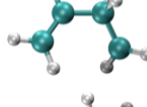
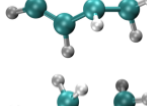
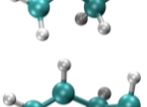
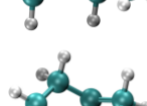
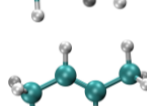
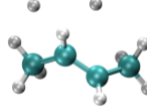
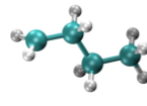
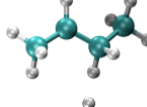
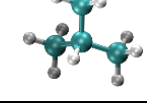
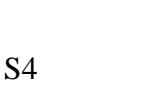
Section S1. Species List in the Nanoreactor Kinetic Model.

Table S1 documents the information of 53 species in the nanoreactor kinetic model, including their molecular formula (C_mH_n), a shortened-version of labels presented in **Figure 2**, modified SMILES labels in the Cantera¹ kinetic model (.cti) file, and their molecular structures optimized at UB3LYP/6-31G** level of theory. Noted that the modified SMILES labels differ from the conventional ones in two aspects, which are 1) the hydrogen (H) atoms are explicitly included in the SMILES string, and 2) species charge and spin multiplicity are denoted as the postfix {charge, spin multiplicity}. The charge and spin multiplicity assignment of each species and reaction paths are detailed in **Section S4**.

Table S1. List of 53 species in the nanoreactor kinetic model.

No.	Formula	Fig. 2 label ^a	Modified SMILES label in the Cantera kinetic model (.cti) file	Molecular structure
1	H	H	[H] {0, 2}	
2	H ₂	H ₂	[H] [H] {0, 1}	
3	CH ₂	CH ₂	[H] [C] [H] {0, 3}	
4	CH ₂	CH ₂ (S)	[H] [C] [H] {0, 1}	
5	CH ₃	CH ₃	[H] [C] ([H]) [H] {0, 2}	
6	CH ₄	CH ₄	[H] [C] ([H]) ([H]) [H] {0, 1}	
7	C ₂ H	C ₂ H	[H] [C] [C] {0, 2}	
8	C ₂ H ₂	C ₂ H ₂	[H] [C] [C] [H] {0, 1}	
9	C ₂ H ₂	H ₂ CC	[H] [C] ([H]) [C] {0, 1}	
10	C ₂ H ₃	C ₂ H ₃	[H] [C] [C] ([H]) [H] {0, 2}	
11	C ₂ H ₄	C ₂ H ₄	[H] [C] ([H]) [C] ([H]) [H] {0, 1}	
12	C ₂ H ₄	CH ₃ CH(T)	[H] [C] [C] ([H]) ([H]) [H] {0, 3}	
13	C ₂ H ₄	C ₂ H ₄ (T)	[H] [C] ([H]) [C] ([H]) [H] {0, 3}	
14	C ₂ H ₅	C ₂ H ₅	[H] [C] ([H]) [C] ([H]) ([H]) [H] {0, 2}	

15	C ₂ H ₆	C ₂ H ₆	[H] [C] ([H]) ([H]) [C] ([H]) ([H]) [H] {0,1}	
16	C ₃ H ₄	C ₃ H ₄ -R(T)	[H] [C] [C] ([H]) [C] ([H]) [H] {0,3}	
17	C ₃ H ₄	<i>c</i> -C ₃ H ₄	[H] [C] 1 [C] ([H]) [C] 1 ([H]) [H] {0,1}	
18	C ₃ H ₄	C ₃ H ₄ -p	[H] [C] [C] [C] ([H]) ([H]) [H] {0,1}	
19	C ₃ H ₄	C ₃ H ₄ -a	[H] [C] ([H]) [C] [C] ([H]) [H] {0,1}	
20	C ₃ H ₅	C ₃ H ₅ -1-2	[H] [C] ([H]) [C] [C] ([H]) ([H]) [H] {0,2}	
21	C ₃ H ₅	C ₃ H ₅ -1-1	[H] [C] [C] ([H]) [C] ([H]) ([H]) [H] {0,2}	
22	C ₃ H ₅	C ₃ H ₅ -a	[H] [C] ([H]) [C] ([H]) [C] ([H]) [H] {0,2}	
23	C ₃ H ₆	C ₃ H ₆	[H] [C] ([H]) [C] ([H]) [C] ([H]) ([H]) [H] {0,1}	
24	C ₃ H ₆	C ₃ H ₆ -3m(T)	[H] [C] ([H]) [C] ([H]) ([H]) [C] ([H]) [H] {0,3}	
25	C ₃ H ₆	C ₃ H ₆ -R(T)	[H] [C] [C] ([H]) ([H]) [C] ([H]) ([H]) [H] {0,3}	
26	C ₃ H ₆	C ₃ H ₆ (T)	[H] [C] ([H]) [C] ([H]) [C] ([H]) ([H]) [H] {0,3}	
27	C ₃ H ₆	<i>c</i> -C ₃ H ₆	[H] [C] 1 ([H]) [C] ([H]) ([H]) [C] 1 ([H]) [H] {0,1}	
28	C ₃ H ₇	<i>n</i> -C ₃ H ₇	[H] [C] ([H]) [C] ([H]) ([H]) [C] ([H]) ([H]) [H] {0,2}	
29	C ₃ H ₇	<i>i</i> -C ₃ H ₇	[H] [C] ([C] ([H]) ([H]) [H]) [C] ([H]) ([H]) [H] {0,2}	
30	C ₃ H ₈	C ₃ H ₈	[H] [C] ([H]) ([H]) [C] ([H]) ([H]) [C] ([H]) ([H]) [H] {0,1}	
31	C ₄ H ₃	<i>n</i> -C ₄ H ₃	[H] [C] [C] [C] ([H]) [C] [H] {0,2}	

32	C ₄ H ₄	C ₄ H ₄ -R(S)	[H] [C] ([H]) [C] ([H]) [C] ([H]) [C] {0,1}	
33	C ₄ H ₄	C ₄ H ₄	[H] [C] [C] [C] ([H]) [C] ([H]) [H] {0,1}	
34	C ₄ H ₅	<i>n</i> -C ₄ H ₅	[H] [C] [C] ([H]) [C] ([H]) [C] ([H]) [H] {0,2}	
35	C ₄ H ₆	C ₄ H ₆	[H] [C] ([H]) [C] ([H]) [C] ([H]) [C] ([H]) [H] {0,1}	
36	C ₄ H ₇	C ₄ H ₇ -1-3	[H] [C] ([H]) [C] ([H]) [C] ([H]) [C] ([H]) ([H]) [H] {0,2}	
37	C ₄ H ₇	C ₄ H ₇ -1,4	[H] [C] [C] ([H]) ([H]) [C] ([H]) ([H]) [C] ([H]) [H] {0,2}	
38	C ₄ H ₇	C ₄ H ₇ -1-4	[H] [C] ([H]) [C] ([H]) [C] ([H]) ([H]) [C] ([H]) [H] {0,2}	
39	C ₄ H ₇	C ₄ H ₇ -1-1	[H] [C] [C] ([H]) [C] ([H]) ([H]) [C] ([H]) ([H]) [H] {0,2}	
40	C ₄ H ₈	C ₄ H ₈ -4m(T)	[H] [C] ([H]) [C] ([H]) ([H]) [C] ([H]) ([H]) [C] ([H]) [H] {0,3}	
41	C ₄ H ₈	C ₄ H ₈ -1	[H] [C] ([H]) [C] ([H]) [C] ([H]) ([H]) [C] ([H]) ([H]) [H] {0,1}	
42	C ₄ H ₈	C ₄ H ₈ -2R(T)	[H] [C] ([H]) [C] ([H]) ([H]) [C] ([H]) [C] ([H]) ([H]) [H] {0,3}	
43	C ₄ H ₈	C ₄ H ₈ -2	[H] [C] ([C] ([H]) [C] ([H]) ([H]) [H]) [C] ([H]) ([H]) [H] {0,1}	
44	C ₄ H ₈	C ₄ H ₈ -2(T)	[H] [C] ([C] ([H]) [C] ([H]) ([H]) [H]) [C] ([H]) ([H]) [H] {0,3}	
45	C ₄ H ₉	<i>n</i> -C ₄ H ₉	[H] [C] ([H]) [C] ([H]) ([H]) [C] ([H]) ([H]) [C] ([H]) ([H]) [H] {0,2}	
46	C ₄ H ₉	<i>s</i> -C ₄ H ₉	[H] [C] ([C] ([H]) ([H]) [H]) [C] ([H]) ([H]) [C] ([H]) ([H]) [H] {0,2}	
47	C ₄ H ₁₀	<i>i</i> -C ₄ H ₁₀	[H] [C] ([H]) ([H]) [C] ([H]) ([C] ([H]) ([H]) [H]) [C] ([H]) ([H]) [H] {0,1}	

48	C ₅ H ₅	C ₅ H ₅	[H][C][C][C]([H])[C]([H])[C]([H])[H]{0,2}	
49	C ₅ H ₆	C ₅ H ₆	[H][C]([H])[C][C]([H])[C]([H])[C]([H])[H]{0,1}	
50	C ₅ H ₁₁	<i>i</i> -C ₅ H ₁₁	[H][C]([C]([H])([H])[H])[C]([H])([C]([H])([H])[H])[C]([H])([H])[H]{0,2}	
51	C ₅ H ₁₂	<i>i</i> -C ₅ H ₁₂	[H][C]([H])([H])[C]([H])([H])[C]([H])([C]([H])([H])[H])[C]([H])([H])[H]{0,1}	
52	C ₆ H ₉	C ₆ H ₉	[H][C]([H])[C]([H])[C]([H])[C][C]([H])([H])[C]([H])([H])[H]{0,2}	
53	C ₆ H ₁₀	C ₆ H ₁₀	[H][C]([H])[C]([H])[C]([H])[C]([H])[C]([H])([H])[C]([H])([H])[H]{0,1}	

^a Corresponding label in **Fig. 2** of the main text.

Section S2. Information about Literature Kinetic Models.

Table S2 shows the information about four literature kinetic models used in this work. These models are used for validating the nanoreactor kinetic model.

Table S2. Information about four literature kinetic models used in this work.

Kinetic model	No. of species	No. of reactions	Reference	Additional comments
GRI Mech 3.0	53	325	Ref. 2	An optimized reaction model designed for natural gas combustion.
ABF	101	544	Ref. 3	A model which predicts well the fuel rich combustion behavior of small hydrocarbons (e.g., ethane, ethylene, and acetylene).
USC Mech II	111	784	Ref. 4	A kinetic model that generally captures the combustion behaviors of H ₂ /CO/C ₁ -C ₄ hydrocarbons.
AramcoMech 3.0	581	3037	Ref. 5	A recently developed kinetic model for H ₂ /CO/C ₁ -C ₄ hydrocarbon combustion.

Section S3. Reaction Discovery Runs and an Example of Temperature Plot.

Figure S1 shows an example of temperature evolution during one *ab initio* molecular dynamics (AIMD) simulation at thermostat temperature of $T_{\text{eq}} = 1500$ K. As can be seen, during each piston compression event, the system temperature, which is calculated from the kinetic energy, can reach much higher values than equilibrium (because of the finite response time of the thermostat). After the compression force is released, the temperature is quenched back to the target T_{eq} . **Table S3** shows a list of all nanoreactor discovery runs.

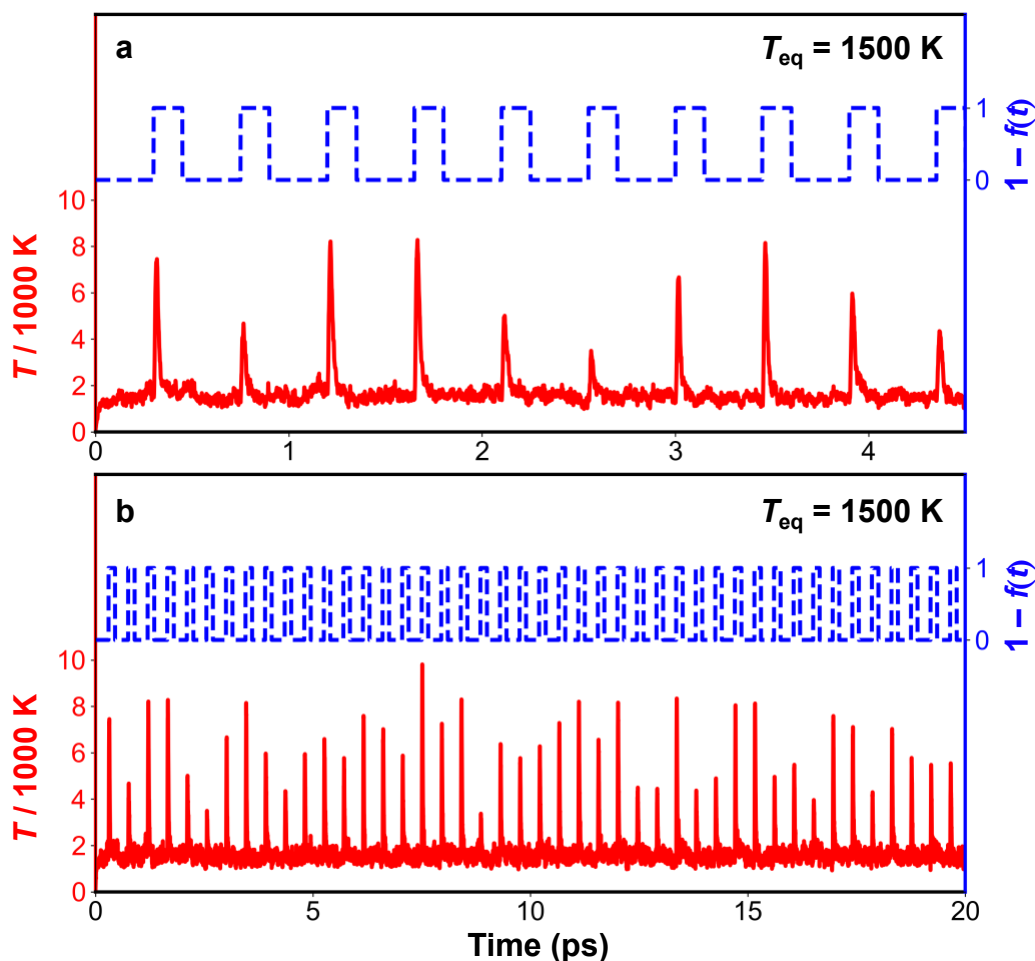


Figure S1. Plot of temperature evolution in one AIMD simulation at thermostat temperature $T_{\text{eq}} = 1500$ K over (a) the first 4.5 ps simulation time (corresponding to 10 piston compression cycles) and (b) the entire 20 ps simulation time. Solid red line: temperature calculated from the kinetic energy; dashed blue line: $1 - f(t)$ where $f(t)$ is a periodic forcing function modulating the compression as defined in Eqn. (3) in the main text. In both panels, the compression force is on when $1 - f(t) = 1$ and compression is off when $1 - f(t) = 0$.

Table S3. List of all nanoreactor discovery runs performed in this study.

Reactant molecules/radicals	Method/Basis set	Thermostat temperature, T_{eq} (K)	No. of runs	Simulation time in each run (ps)	No. of unique species discovered ^a	No. of unique reactions discovered ^a
8CH ₄ , 3H	UB3LYP/3-21G	1500	10	20	6	10
8CH ₄ , 3H	UB3LYP/3-21G	2000	10	20	8	15
8CH ₄ , 3H	UB3LYP/3-21G	2500	10	20	14	35
8CH ₄ , 3H	UB3LYP/3-21G	3000	10	20	26	77
8CH ₄ , 3H	UB3LYP/3-21G	3500	10	20	47	142

^a Unique species and reactions discovered under different thermostat temperatures (T_{eq}) may overlap.

Section S4. Charge and Spin Multiplicity Assignment for Species and Reactions.

In the AIMD reaction discovery phase, reaction paths are extracted and saved with 40 frames (including reactant and product species) across the reaction event time interval. In order to extract the reacting atoms from the AIMD discovery run for future refinement, one needs to determine the charge and spin of the reacting subsystem, as well as the identities of the atoms which will be included. As discussed in the main text, we determine the identities of the atoms which are included in the subsystem by collecting all atoms which are involved in bond-making or bond-breaking events during the reaction event time interval. All molecules which involve these atoms are then included in the subsequent refinement calculations aimed at determining minimal energy paths.

Once the atoms involved in the reacting subsystem have been determined, we need to also determine a charge and spin multiplicity for the subsystem. These are determined by analyzing the electronic structure of the subsystem over the reactive event. We first determine the charge through two steps. First, the atomic charge for each atom in the reactive subsystem is assigned as the mean Mulliken atomic charge⁶ averaged over all frames in the reaction path. Second, the total charge (Q) is computed by summing the averaged atomic charges over all atoms in the subsystem and rounding the sum to the nearest integer. We then compute the total spin density ($2S$) of the reactive subsystem (which is equivalent to the total number of unpaired electrons), again with a two-step approach: 1) the spin density of each atom is assigned as the Mulliken atomic spin density⁶ averaged over all frames in the reaction path; 2) the total spin density ($2S$) of the subsystem is computed by summing the averaged atomic spin densities over all atoms in the subsystem and rounding to its nearest integer. Care has been taken to make sure the total charge and spin multiplicity values are consistent with the number of electrons N_{elec} in the reaction, thus fulfilling the following relationship.

$$(N_{elec} - Q + 2S) \equiv 0 \pmod{2}$$

We also need to assign the charge/spin of individual reactant and/or product species in order to assign species labels and to compute thermodynamic corrections (such as the electronic contribution to the partition function). This is accomplished in a single step by taking the sum of the Mulliken atomic charges or spin densities associated with this species and rounding to the nearest integer. Again, we ensure that the total charge and spin are consistent with the number of electrons in the species. Lastly, we note that one should be very careful about the choice of charge and spin partition scheme. The Mulliken population analysis⁶ used here can be sensitive to the basis set used. The resulting Mulliken charges and spin densities will be of little value when the basis set is large (and particularly with diffuse functions). However, given the modest basis sets currently used in the nanoreactor workflow, we expect Mulliken population analysis will provide efficient and reasonable estimations on charges and spin densities (see **Table S1** which contains the modified SMILES strings for species along with their charge and spin multiplicity values). When larger basis sets are used, it will be necessary to find alternative methods for charge and spin density analysis (and we are working to implement such methods).

In the discovery phase, the charge and spin multiplicity values of species and reaction paths are saved to the database for future use. For example, the species charge and multiplicity will be used as inputs in endpoint relaxation and thermochemistry calculations, and the reaction charge and multiplicity will be used in path refinement and transition state optimizations.

Section S5. Thermochemistry Calculations.

In **Section 2.3**, we briefly discussed our procedure for computing thermodynamic corrections. Additional details are provided in this section. The thermochemical properties of reactants, products, and transition state structures are derived from the expression for molecular partition function, which is assumed to be a product of translational, rotational, vibrational, and electronic partition functions.⁷

$$Q = Q_{\text{trans}}Q_{\text{rot}}Q_{\text{vib}}Q_{\text{elec}} \quad (\text{S1})$$

where Q_{trans} is the translational partition function, Q_{rot} , Q_{vib} , and Q_{elec} are rotational, vibrational, and electronic partition functions, respectively. Following Eqn. (S1), the thermochemical properties of a species can be calculated as

$$H = H_{\text{trans}} + H_{\text{rot}} + H_{\text{vib}} + H_{\text{elec}} \quad (\text{S2})$$

$$S = S_{\text{trans}} + S_{\text{rot}} + S_{\text{vib}} + S_{\text{elec}} \quad (\text{S3})$$

$$C_p = C_{p,\text{trans}} + C_{p,\text{rot}} + C_{p,\text{vib}} + C_{p,\text{elec}} \quad (\text{S4})$$

In the following subsections, we describe the contribution from each partition function.

S5.1. Translational Contributions.

The translational partition function Q_{trans} and the contributions to H , S , and C_p are

$$Q_{\text{trans}} = \left(\frac{2\pi mk_B T}{h^2} \right)^{\frac{3}{2}} V \quad (\text{S5})$$

$$H_{\text{trans}} = \frac{5}{2} RT \quad (\text{S6})$$

$$S_{\text{trans}} = \frac{5}{2} R + R \ln \left[\left(\frac{2\pi mk_B T}{h^2} \right)^{\frac{3}{2}} \frac{V}{N} \right] \quad (\text{S7})$$

$$C_{p,\text{trans}} = \frac{5}{2} R \quad (\text{S8})$$

where k_B is the Boltzmann constant, R is the universal gas constant, h is the Planck constant, m is the molecular mass, T is the temperature, V is the system volume, and N is the number of particles in the system. The term $\frac{V}{N}$ can be expressed as $\frac{k_B T}{P}$ for ideal gases.

S5.2. Rotational Contributions.

The rotational partition function Q_{rot} and its contributions to H , S , and C_p are described as follows. For non-linear polyatomic molecules, they are defined as

$$Q_{\text{rot}} = \frac{\pi^{1/2}}{\sigma} \left[\frac{(k_B T)^3}{B_x B_y B_z} \right]^{1/2} \quad (\text{S9})$$

$$H_{\text{rot}} = \frac{3}{2} RT \quad (\text{S10})$$

$$S_{\text{rot}} = \frac{3}{2} R + R \ln \left[\frac{\pi^{1/2}}{\sigma} \left(\frac{(k_B T)^3}{B_x B_y B_z} \right)^{1/2} \right] \quad (\text{S11})$$

$$C_{p,\text{rot}} = \frac{3}{2} R \quad (\text{S12})$$

$$B_x = \frac{h}{8\pi I_x c} \quad (\text{S13})$$

where σ is the symmetry number of the species optimized geometries, B_x (in Eqn. S13), B_y and B_z are the rotational constants along three principal axes of rotation, and I_x is the moment of inertia along one of the principal axes of rotation. For linear-polyatomic molecules, Eqns. (S9-S12) can be simplified as

$$Q_{\text{rot}} = \frac{k_B T}{\sigma B} \quad (\text{S14})$$

$$H_{\text{rot}} = RT \quad (\text{S15})$$

$$S_{\text{rot}} = R \left[1 + \ln \left(\frac{k_B T}{\sigma B} \right) \right] \quad (\text{S16})$$

$$C_{p,\text{rot}} = R \quad (\text{S17})$$

S5.3. Vibrational Contributions.

The vibrational partition function Q_{vib} and its contributions to H , S , and C_p are defined as follows.

$$Q_{\text{vib}} = \prod_{i=1}^{N_{\text{vib}}} \frac{e^{-h\nu_i/2k_B T}}{1 - e^{-h\nu_i/k_B T}} = \prod_{i=1}^{N_{\text{vib}}} \frac{e^{-\tilde{\omega}_i/2\tilde{k}T}}{1 - e^{-\tilde{\omega}_i/\tilde{k}T}} \quad (\text{S18})$$

$$H_{\text{vib}} = R \sum_{i=1}^{N_{\text{vib}}} \left(\frac{h\nu_i}{2k_B} + \frac{h\nu_i/k_B}{e^{h\nu_i/k_B T} - 1} \right) = hcN_A \sum_{i=1}^{N_{\text{vib}}} \left(\frac{\tilde{\omega}_i}{2} + \frac{\tilde{\omega}_i}{e^{\tilde{\omega}_i/\tilde{k}T} - 1} \right) \quad (\text{S19})$$

$$\begin{aligned} S_{\text{vib}} &= R \sum_{i=1}^{N_{\text{vib}}} \left[\frac{h\nu_i/k_B T}{e^{h\nu_i/k_B T} - 1} - \ln \left(1 - e^{-h\nu_i/k_B T} \right) \right] \\ &= hcN_A \sum_{i=1}^{N_{\text{vib}}} \left[\frac{\tilde{\omega}_i/T}{e^{\tilde{\omega}_i/\tilde{k}T} - 1} - \tilde{k} \ln \left(1 - e^{-\tilde{\omega}_i/\tilde{k}T} \right) \right] \end{aligned} \quad (\text{S20})$$

$$\begin{aligned} C_{p,\text{vib}} &= R \sum_{i=1}^{N_{\text{vib}}} \left(\frac{h\nu_i}{k_B T} \right)^2 \frac{e^{h\nu_i/k_B T}}{(e^{h\nu_i/k_B T} - 1)^2} \\ &= R \sum_{i=1}^{N_{\text{vib}}} \frac{\tilde{\omega}_i^2}{\tilde{k}T^2} \frac{e^{\tilde{\omega}_i/\tilde{k}T}}{(e^{\tilde{\omega}_i/\tilde{k}T} - 1)^2} \end{aligned} \quad (\text{S21})$$

The first equality in each equation is expressed in terms of vibrational frequencies ν_i (with units of s^{-1}). For the convenience, we introduce the second equality which is given in terms of frequencies $\tilde{\omega}_i$ (with units of cm^{-1} , i.e. wavenumbers). In the second equality, $\tilde{k} = k_B/hc$ is Boltzmann's constant in $\text{cm}^{-1}\text{K}^{-1}$, c is the speed of light, and N_A is Avogadro's number. N_{vib} represents the total number of vibrational modes in a molecule. For a linear polyatomic molecule, $N_{\text{vib}} = 3N_{\text{atom}} - 5$, while for a non-linear polyatomic molecule $N_{\text{vib}} = 3N_{\text{atom}} - 6$. Eqns. (S19-S21) generally work for vibrations that can be approximately treated as harmonic modes, but they do not work well for low-frequency modes. Instead, we treat those low-frequency vibrations (frequency threshold being mentioned later) as rotational modes. A modification to the entropy term is added using Grimme's quasi-rigid rotor harmonic oscillator (RRHO) method⁸ combined with a damping function⁹ to switch between the rotational and vibrational regimes. This entropy modification is defined as

$$S_{\text{RRHO}} = w(\tilde{\omega}_i)S_{i,\text{vib}} + [1 - w(\tilde{\omega}_i)]S_{i,\text{rot}} \quad (\text{S22})$$

$$w(\tilde{\omega}_i) = \frac{1}{1 + (\tilde{\omega}_0/\tilde{\omega}_i)^\alpha} \quad (\text{S23})$$

where we choose $\tilde{\omega}_0$ to be 100 cm^{-1} and α to be 4, whose values are all taken from Grimme's work.⁸ The $S_{i,\text{vib}}$ term corresponds to the single term in Eqn. (S20), and $S_{i,\text{rot}}$ is the 1-D equivalent of rotational contribution to entropy. The $S_{i,\text{rot}}$ along with its effective moment of inertia (μ') is described as

$$S_{i,\text{rot}} = \frac{R}{2} \left[1 + \ln \left(\frac{8\pi^3 \mu' k_B T}{h^2} \right) \right] \quad (\text{S24})$$

$$\mu' = \frac{\mu B_{\text{avg}}}{\mu + B_{\text{avg}}} \quad (\text{S25})$$

$$\mu = \frac{h}{8\pi^2 c \tilde{\omega}_i} \quad (\text{S26})$$

where B_{avg} ($= 10^{-44} \text{ kg}\cdot\text{m}^2$) is the average rotational constant, whose value is also taken from Grimme's work.⁸

For transition state geometries, small imaginary frequencies lower than $30i \text{ cm}^{-1}$ are treated as real modes with the same magnitude. The large-amplitude imaginary frequencies (including the largest-amplitude mode that is expected to correspond to the reaction coordinate) are neglected in the thermochemistry calculations. Moreover, the transition state geometries are optimized based on minimization of energy gradient. As stated in the text, this may not guarantee a first-order saddle point on a reaction path. This point is further illustrated in **Figure S2**, which shows the distributions of imaginary frequency amplitudes with respect to number of imaginary frequencies (N_{imag}) for (a) all 134 reaction paths and (b) bimolecular reaction paths most of which were found to have a distinct barrier after path refinement. As seen in both **Figure S2a** and **S2b**, for the reaction paths that have 1 imaginary frequency mode ($N_{\text{imag}} = 1$), the distribution leans towards considerably large imaginary frequencies ($\sim O(10^3) \text{ cm}^{-1}$) which may represent the normal mode along the reaction coordinate. When N_{imag} increases, the largest imaginary frequencies peak between $O(10^2)$ to $O(10^3) \text{ cm}^{-1}$, which is similar to (but somewhat smaller than) the $N_{\text{imag}} = 1$ case. Most of the other imaginary frequencies (i.e., 2nd or 3rd largest-amplitudes) are found to be quite small ($< O(10^2) \text{ cm}^{-1}$). As the force constant matrix is computed by finite difference of analytic gradients, this may be indicative of numerical noise in the finite difference procedure. We further

observe that the bimolecular reaction transition states (**Figure S2b**) show a more distinct peak in the $N_{\text{imag}} = 1$ distribution than the entire distribution (**Figure S2a**). Overall, the results in **Figure S2** suggest that even though the current nanoreactor transition state optimization approach may not always guarantee first-order saddle points along a reaction path, the issue is not pronounced since most of the additional imaginary frequencies are small and likely due to numerical noise in the finite difference procedure used to generate the force constant matrix.

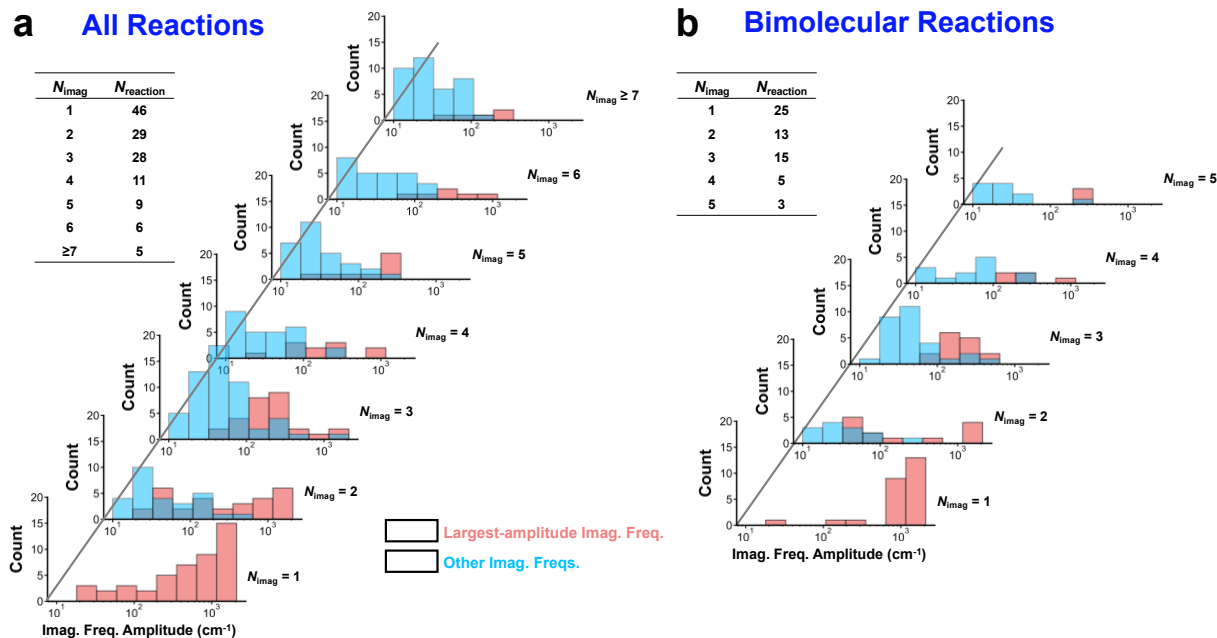
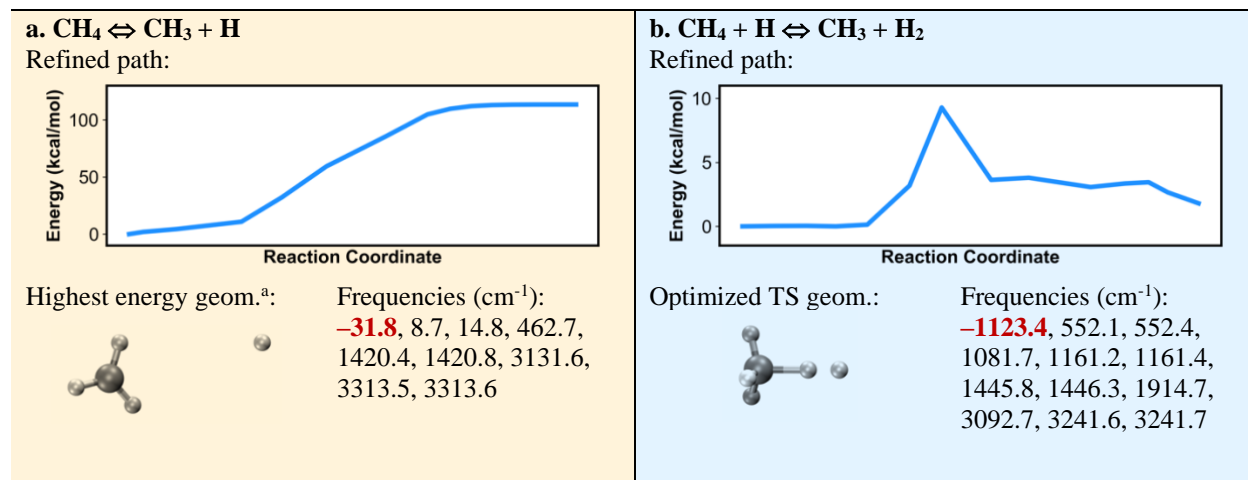


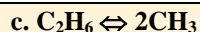
Figure S2. Distributions of imaginary frequency amplitudes with respect to number of imaginary frequencies (N_{imag}) for (a) all the 134 reaction transition states and (b) the bimolecular reaction transition states. The inset table shows number of reaction paths (N_{reaction}) that have transition state configurations with N_{imag} varying. The red histogram corresponds to the distribution of the largest-amplitude imaginary frequency for each transition state configuration, with the total count equal to N_{reaction} under a given N_{imag} distribution. The blue histogram corresponds to the distribution of other imaginary modes (i.e., 2nd-, 3rd-, ... largest imaginary frequency modes in each transition state configuration), with the total count equal to $(N_{\text{imag}} - 1) \times N_{\text{reaction}}$ under a given N_{imag} distribution.

We further show in **Table S4** the refined path, optimized transition state geometry and its vibrational frequencies in the 10 most important reactions for CH₄ destruction found from sensitivity analysis (**Figure 5**). These 10 reactions include 5 unimolecular reactions (left column) and 5 bimolecular reactions (right column). From the results of the refined paths, 3 unimolecular decomposition reactions (left column, a. CH₄ ⇌ CH₃ + H, c. C₂H₆ ⇌ 2CH₃, and e. C₂H₆ ⇌ C₂H₅

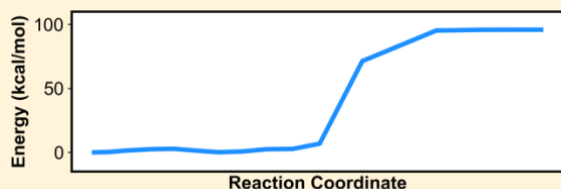
+ H) are found to be barrierless. Their putative “transition state” configurations are optimized from the last point (i.e., the highest-energy frame) in the refined paths and are not first-order saddle points (i.e., small imaginary frequencies are found in their “TS” frequencies). On the other hand, 2 radical H-elimination reactions (left column, g. $\text{C}_2\text{H}_5 \rightleftharpoons \text{C}_2\text{H}_4 + \text{H}$, and i. $\text{C}_2\text{H}_3 \rightleftharpoons \text{C}_2\text{H}_2 + \text{H}$) and all 5 bimolecular reactions (right column, b. $\text{CH}_4 + \text{H} \rightleftharpoons \text{CH}_3 + \text{H}_2$, d. $\text{C}_2\text{H}_6 + \text{H} \rightleftharpoons \text{C}_2\text{H}_5 + \text{H}_2$, f. $\text{C}_2\text{H}_6 + \text{CH}_3 \rightleftharpoons \text{C}_2\text{H}_5 + \text{CH}_4$, h. $\text{C}_2\text{H}_4 + \text{H} \rightleftharpoons \text{C}_2\text{H}_3 + \text{H}_2$, and j. $\text{C}_2\text{H}_4 + \text{CH}_3 \rightleftharpoons \text{C}_2\text{H}_3 + \text{CH}_4$) contain a reaction barrier, according to their refined paths. We found 6 out of 7 of their optimized transition state geometries contain only one imaginary frequency with the amplitude larger than 200 cm^{-1} , reaffirming that they are first-order saddle points. Only the TS of Reaction f. $\text{C}_2\text{H}_6 + \text{CH}_3 \rightleftharpoons \text{C}_2\text{H}_5 + \text{CH}_4$ contains two significant imaginary frequencies, which is probably worth future investigation. Nevertheless, the results in **Figure S2** and **Table S4** validate the current transition state optimization workflow in the *ab initio* nanoreactor. Although some inaccuracy might be introduced in the rate constant estimation, we will show later that the overall impact on kinetic modeling is not significant.

Table S4. Refined reaction path, optimized transition state geometry and its vibrational frequencies (imaginary frequencies are listed as negative values) in 10 most important reactions for CH_4 destruction found from sensitivity analysis (**Fig. 5** in the main text). The left column contains unimolecular reactions, including three unimolecular decomposition reactions which are found to be barrierless (a. $\text{CH}_4 \rightleftharpoons \text{CH}_3 + \text{H}$, c. $\text{C}_2\text{H}_6 \rightleftharpoons 2\text{CH}_3$, and e. $\text{C}_2\text{H}_6 \rightleftharpoons \text{C}_2\text{H}_5 + \text{H}$), and two radical hydrogen-elimination reactions which contains small barriers and presumably a transition state configuration (g. $\text{C}_2\text{H}_5 \rightleftharpoons \text{C}_2\text{H}_4 + \text{H}$, and i. $\text{C}_2\text{H}_3 \rightleftharpoons \text{C}_2\text{H}_2 + \text{H}$). The right column contains bimolecular reactions which have a barrier and presumably a transition state configuration (b. $\text{CH}_4 + \text{H} \rightleftharpoons \text{CH}_3 + \text{H}_2$, d. $\text{C}_2\text{H}_6 + \text{H} \rightleftharpoons \text{C}_2\text{H}_5 + \text{H}_2$, f. $\text{C}_2\text{H}_6 + \text{CH}_3 \rightleftharpoons \text{C}_2\text{H}_5 + \text{CH}_4$, h. $\text{C}_2\text{H}_4 + \text{H} \rightleftharpoons \text{C}_2\text{H}_3 + \text{H}_2$, and j. $\text{C}_2\text{H}_4 + \text{CH}_3 \rightleftharpoons \text{C}_2\text{H}_3 + \text{CH}_4$).





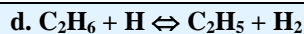
Refined path:



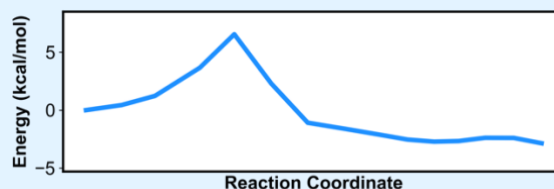
Highest energy geom.^a:



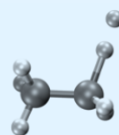
Frequencies (cm^{-1}):
-47.3, -21.5, 22.0, 39.9,
 41.8, 68.0, 463.1, 467.8,
 1418.5, 1420.2, 1420.6,
 1421.5, 3130.9, 3131.2,
 3312.8, 3312.9, 3313.4,
 3313.8



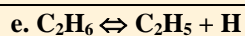
Refined path:



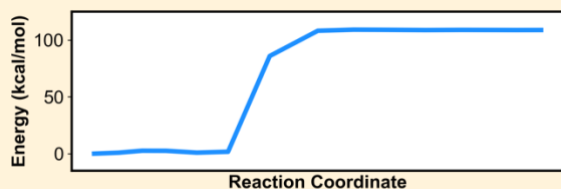
Optimized TS geom.:



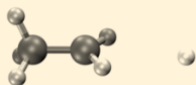
Frequencies (cm^{-1}):
-1222.5, 191.4, 317.9,
 573.1, 843.0, 886.9,
 1028.1, 1124.8, 1216.5,
 1245.4, 1260.5, 1418.5,
 1481.7, 1503.2, 1506.5,
 1644.2, 3026.1, 3085.8,
 3099.4, 3117.1, 3178.5



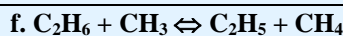
Refined path:



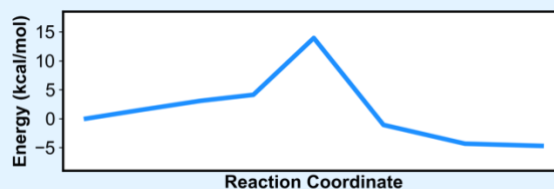
Highest energy geom.^a:



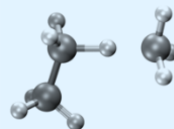
Frequencies (cm^{-1}):
-135.5, **-75.4**, 38.3,
 121.8, 447.0, 826.2,
 979.3, 1071.7, 1190.7,
 1414.5, 1480.2, 1493.1,
 1501.1, 2968.5, 3049.6,
 3106.2, 3165.9, 3266.8



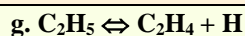
Refined path:



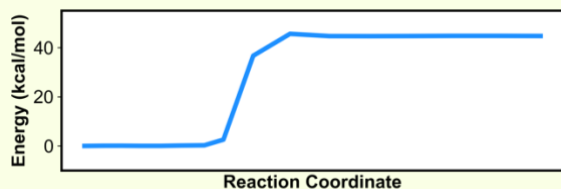
Optimized TS geom.:



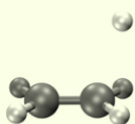
Frequencies (cm^{-1}):
-1596.8, **-207.9**, 36.1,
 141.9, 296.5, 478.6,
 567.6, 671.4, 909.3,
 972.6, 1035.1, 1141.8,
 1164.4, 1194.1, 1406.1,
 1409.8, 1430.9, 1463.3,
 1467.5, 1485.7, 1509.0,
 1514.0, 3032.8, 3078.8,
 3083.1, 3093.6, 3110.9,
 3162.6, 3214.6, 3216.0



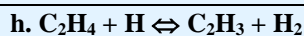
Refined path:



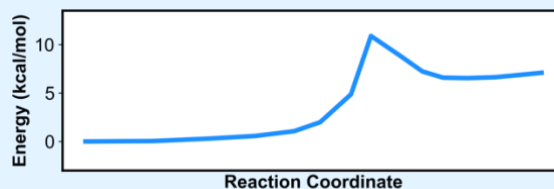
Optimized TS geom.:



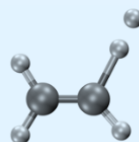
Frequencies (cm^{-1}):
-323.0, 234.2, 306.5,
 830.9, 950.7, 974.9,
 1056.9, 1240.9, 1372.9,
 1481.6, 1677.8, 3151.3,
 3164.2, 3228.9, 3254.6



Refined path:



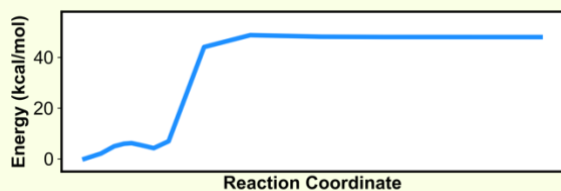
Optimized TS geom.:



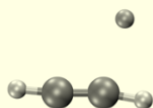
Frequencies (cm^{-1}):
-981.2, 287.8, 354.2,
 831.0, 885.4, 952.3,
 979.5, 1108.3, 1173.1,
 1409.9, 1658.6, 2150.8,
 3106.4, 3192.7, 3217.4

i. C₂H₃ ⇌ C₂H₂ + H

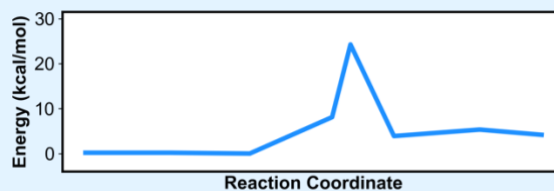
Refined path:



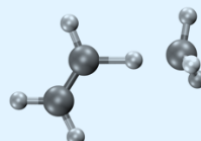
Optimized TS geom.:


 Frequencies (cm⁻¹):
-433.3, 317.0, 579.0,
 632.3, 768.5, 793.9,
 2039.4, 3433.5, 3524.6
j. C₂H₄ + CH₃ ⇌ C₂H₃ + CH₄

Refined path:



Optimized TS geom.:


 Frequencies (cm⁻¹):
-1601.6, 18.7, 153.4,
 241.6, 457.1, 540.4,
 580.1, 898.4, 920.6,
 968.5, 1188.0, 1204.8,
 1279.7, 1397.5, 1426.8,
 1461.9, 1477.9, 1679.5,
 3075.4, 3103.2, 3183.3,
 3192.9, 3204.2, 3209.7

^aBarrierless reactions a. CH₄ ⇌ CH₃ + H, c. C₂H₆ ⇌ 2CH₃, and e. C₂H₆ ⇌ C₂H₅ + H do not contain a transition state, so we denote them as “highest-energy geometry” on the refined path (i.e., the endpoints on the refined path).

S5.4. Electronic Contributions.

The electronic partition function Q_{elec} and its contributions to H , S , and C_p are defined as follows.

$$Q_{\text{elec}} = g e^{E_{\text{elec}}/k_B T} \quad (\text{S27})$$

$$H_{\text{elec}} = E_{\text{elec}} \quad (\text{S28})$$

$$S_{\text{elec}} = R \ln(g) \quad (\text{S29})$$

$$C_{p,\text{elec}} = 0 \quad (\text{S30})$$

where g is the degeneracy (i.e., spin multiplicity) of the electronic ground state, and E_{elec} is the ground state energy including the correction from Yamaguchi spin projection^{10,11} if necessary. Specifically, Yamaguchi spin projection is used in this work to correct the energy caused by spin contamination in unrestricted density functional (UB3LYP) calculations. It treats the interactions of localized α and β spins using the Heisenberg Hamiltonian

$$\hat{H} = -2J_{\alpha\beta} \left(-\hat{S}^2 + \hat{S}_\alpha^2 + \hat{S}_\beta^2 \right) \quad (\text{S31})$$

where \hat{S}^2 is the total spin operator, \hat{S}_α^2 and \hat{S}_β^2 are spin operators for α and β spins, respectively, and $J_{\alpha\beta}$ is an effective exchange integral. As pointed out in the original paper,¹¹ the energy difference between the low-spin (LS) and high-spin (HS) states given by the Heisenberg

Hamiltonian is equal to the LS-HS energy difference obtained from *ab initio* calculations. If no spin contamination is found, the LS-HS energy gap is

$$E_{\text{exact}}^{\text{LS}} - E_{\text{exact}}^{\text{HS}} = 2J_{\alpha\beta} \quad (\text{S32})$$

Otherwise, the LS-HS energy gap is given as

$$E_{\text{BS}}^{\text{LS}} - E^{\text{HS}} = 2J_{\alpha\beta} - J_{\alpha\beta} \left(\langle \hat{S}^2 \rangle_{\text{BS}}^{\text{LS}} - \langle \hat{S}^2 \rangle_{\text{exact}}^{\text{LS}} \right) \quad (\text{S33})$$

where BS stands for a broken-symmetry energy from a spin-contaminated *ab initio* calculation, and it is assumed that spin contamination is negligible in the HS calculation. Furthermore, we derive the spin projection exchange integral $J_{\alpha\beta}$ between LS and HS state as

$$J_{\alpha\beta} = \frac{E_{\text{BS}}^{\text{LS}} - E^{\text{HS}}}{\langle \hat{S}^2 \rangle_{\text{HS}}^{\text{LS}} - \langle \hat{S}^2 \rangle_{\text{BS}}^{\text{LS}}} \quad (\text{S34})$$

Combining Eqns. (S32-S34), the energy correction to the broken-symmetry low-spin state is

$$\begin{aligned} E_{\text{corr}} &= J_{\alpha\beta} \left(\langle \hat{S}^2 \rangle_{\text{BS}}^{\text{LS}} - \langle \hat{S}^2 \rangle_{\text{exact}}^{\text{LS}} \right) \\ &= (E_{\text{BS}}^{\text{LS}} - E^{\text{HS}}) \frac{\langle \hat{S}^2 \rangle_{\text{BS}}^{\text{LS}} - \langle \hat{S}^2 \rangle_{\text{exact}}^{\text{LS}}}{\langle \hat{S}^2 \rangle_{\text{HS}}^{\text{LS}} - \langle \hat{S}^2 \rangle_{\text{BS}}^{\text{LS}}} \end{aligned} \quad (\text{S35})$$

For each optimized geometry of reactant, product, and transition state configuration, spin projection is performed if spin contamination is detected when the value of $\langle \hat{S}^2 \rangle_{\text{BS}}^{\text{LS}}$ exceeds $\langle \hat{S}^2 \rangle_{\text{exact}}^{\text{LS}}$ by a threshold value of 0.1. An additional single-point energy calculation is done for the HS state (i.e., with spin multiplicity $S_{\text{LS}} + 2$, e.g., triplet for a BS singlet, quartet for a BS double). Lastly, the calculated E_{corr} is added to E_{elec} . A general example is shown in **Figure S3**, the histogram of spin contamination errors during the *ab initio* calculation. The error is obtained from comparing the calculated spin value (S_{UB3LYP}) with the exact spin value (S_{exact}) for all the 53 species in the methane kinetic model. Spin errors of most of the species are well within the acceptable range, while two species are detected with spin contamination. **Table S5** summarizes the information of these two species, including their molecular formula, labels, and values of spin-squares, spins, and E_{corr} .

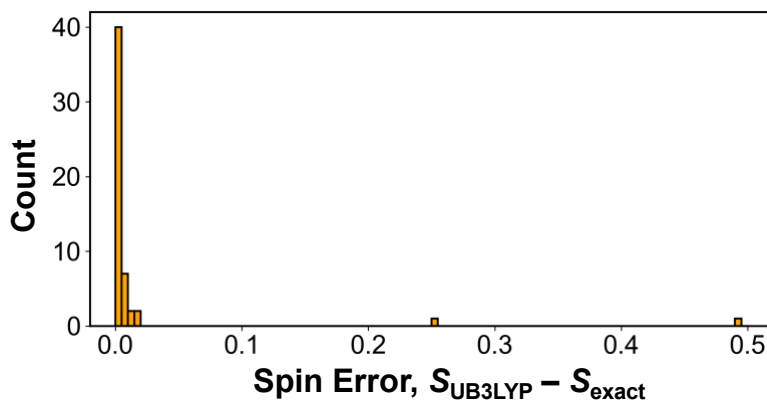


Figure S3. Histogram of the spin contamination errors induced by UB3LYP (S_{UB3LYP}) compared to the exact spin value (S_{exact}) of the minimum structures of all 53 species. The error is obtained from $S_{\text{UB3LYP}} - S_{\text{exact}} = \frac{1}{2} \left(\sqrt{1 + 4\langle S^2 \rangle_{\text{UB3LYP}}} - \sqrt{1 + 4\langle S^2 \rangle_{\text{exact}}} \right)$, where $\langle S^2 \rangle_{\text{UB3LYP}}$ is the calculated $\langle \hat{S}^2 \rangle_{\text{BS}}^{\text{LS}}$ value by UB3LYP functional, and $\langle S^2 \rangle_{\text{exact}}$ is the exact spin-square value of the species.

Table S5. Species detected with spin contamination.

No.	Formula	Fig. 2 label ^a	$\langle S^2 \rangle_{\text{UB3LYP}}$	$\langle S^2 \rangle_{\text{exact}}$	S_{UB3LYP}	S_{exact}	E_{corr} (kcal/mol)
4	CH ₂	CH ₂ (S)	0.736	0.000	0.493	0.000	1.256
37	C ₄ H ₇	C ₄ H ₇ -1,4	1.325	0.750	0.755	0.500	0.980

^a Corresponding label in Fig. 2 of the main text, which is also listed in Table S1.

S5.5. NASA Polynomials.

The computed thermochemical properties (i.e., H , S , and C_p) for reactants, products, and transition state configurations are fitted as polynomial functions of temperature in the form of NASA9 coefficients.¹² The fitting is performed using least squares within 250 – 3000 K temperature range and at 1 bar reference pressure. The NASA9 polynomials of H , S , and C_p take the following form

$$\frac{H(T)}{RT} = -a_0 T^{-2} + a_1 \frac{\ln T}{T} + a_2 + \frac{a_3}{2} T + \frac{a_4}{3} T^2 + \frac{a_5}{4} T^3 + \frac{a_6}{5} T^4 + \frac{a_7}{T} \quad (\text{S36})$$

$$\frac{S(T)}{R} = -\frac{a_0}{2} T^{-2} - a_1 T^{-1} + a_2 \ln T + a_3 T + \frac{a_4}{2} T^2 + \frac{a_5}{3} T^3 + \frac{a_6}{4} T^4 + a_8 \quad (\text{S37})$$

$$\frac{C_p(T)}{R} = a_0 T^{-2} + a_1 T^{-1} + a_2 + a_3 T + a_4 T^2 + a_5 T^3 + a_6 T^4 \quad (\text{S38})$$

The NASA9 coefficients of all 53 species are saved in the Cantera kinetic model (.cti) file.

Section S6. Reaction Rate Parameter Calculations.

The reaction rates are calculated using transition state theory (TST).¹³⁻¹⁵ As mentioned in the main text, the forward rate of the reaction is given by

$$k_f(T) = \frac{k_B T}{h} (c^0)^{(1-n_r)} e^{-\Delta G^\ddagger/RT} \quad (\text{S39})$$

where k_B is the Boltzmann constant, h is the Planck constant, c^0 is the standard molar concentration referenced to 1 atm pressure, n_r is the number of reactant species, and ΔG^\ddagger is the difference of standard Gibbs free energy of the transition state and the reactant. We note that the contribution of vibration partition function to the transition state Gibbs free energy neglects the largest magnitude negative force constant, which corresponds to the reaction coordinate. In the kinetic model, all the forward rates are formulated based on the modified Arrhenius equation

$$k_f(T) = AT^b e^{-E_a/RT} \quad (\text{S40})$$

The parameters A , b , and E_a correspond to

$$A = \frac{k_B}{h} \left(\frac{P^0}{R} \right)^{1-n_r} e^{\Delta S^\ddagger/R} \quad (\text{S41})$$

$$b = n_r \quad (\text{S42})$$

$$E_a = \Delta H^\ddagger \quad (\text{S43})$$

where ΔS^\ddagger and ΔH^\ddagger are the change in standard entropy and enthalpy between reactants and the transition state structures. The reverse rates $k_b(T)$ are computed using microscopic reversibility of the elementary reaction, taking the ratio of forward rate $k_f(T)$ and the equilibrium constant $K_c(T)$.

In this work, we apply transition state theory to all bi-molecular reactions and reactions involving three or more bodies. For unimolecular decomposition reactions (or association reactions in the reverse direction), the high-pressure limit rate coefficient $k_{f,\infty}(T)$ is estimated again using TST, while the low-pressure limit rate coefficient $k_{f,0}(T)$ is estimated using Hinshelwood theory,¹⁶ which considers the internal degrees of freedom of molecules. The original Hinshelwood expression of the low-pressure rate coefficient is given as

$$k_{f,0}(T) = \frac{1}{(s-1)!} \left(\frac{E_0}{RT} \right)^{s-1} Z e^{(-E_0/RT)} \quad (\text{S44})$$

where E_0 is the threshold energy for a molecule to overcome for dissociation, which is assumed to be equal to the forward reaction barrier ΔH^\ddagger . The term $Z e^{(-E_0/RT)}$ is the rate of reaction simply calculated from the collision theory with Z being the collision rate. Here we further assume that

this term can be estimated using transition state theory (Eqn. S39), which is exactly the high-pressure limit rate coefficient. Therefore, the final low-pressure rate coefficient is expressed as

$$k_{f,0}(T) = \frac{1}{(s-1)!} \left(\frac{\Delta H^\ddagger}{RT} \right)^{s-1} k_{f,\infty}(T) \quad (\text{S45})$$

$$s \approx \frac{1}{2} s_{\max}, s_{\max} = N_{\text{vib}} \quad (\text{S46})$$

The factor s in Eqn. (S45) represents the number of effective vibrational modes of a molecule having total energy higher than the threshold dissociation energy barrier ($E_0 = \Delta H^\ddagger$ here). In the nanoreactor, we approximate s to be one half of its maximum possible value s_{\max} , which further corresponds to the total number of vibrational modes in a molecule. Additionally, in the kinetic model following the Cantera¹ format, equations of dissociation reactions in the form of $A \Leftrightarrow B + C$ are modified into $A (+M) \Leftrightarrow B + C (+M)$ where M corresponds to the third body collision partner. The pressure-dependent rate coefficient of $A (+M) \Leftrightarrow B + C (+M)$ is expressed as

$$k_f(T, [M]) = \frac{k_{f,0}(T)[M]}{1 + k_{f,0}(T)[M]/k_{f,\infty}(T)} \quad (\text{S47})$$

Finally, the kinetic model is assembled with the equation and forward rate parameters for each reaction. All the reactions are listed as forward reaction being in the endothermic direction in Cantera format. **Figure S4** shows the comparisons of forward rate coefficients of the 10 most important reactions for CH₄ pyrolysis found from sensitivity analysis (**Figure 5**). Their forward rate coefficients are computed by the nanoreactor, GRI Mech 3.0,² ABF,³ USC Mech II,⁴ and AramcoMech 3.0⁵ kinetic models at 1 atm pressure and 1000–2500 K. Reactions in the left column (**Figure S4a, c, e, g, and i**) are unimolecular and have pressure-dependent rates; those in the right column (**Figure S4b, d, f, h, and j**) are bimolecular and have pressure-independent rates. Furthermore, **Table S6** lists the values of forward rate coefficients in **Figure S4** at two specific temperature $T = 1000$ and 2000 K, respectively. The results in **Figure S4** and **Table S6** indicate that the bimolecular reaction rate coefficients in the nanoreactor kinetic model are mostly within one-order-of-magnitude difference from the rate coefficients in other literature kinetic models, while the deviation of unimolecular pressure-dependent rate coefficients in the nanoreactor model is more pronounced. Future work should focus on improving the accuracy of pressure-dependent rate coefficients, for example, using the RRKM theory.¹⁷⁻¹⁹

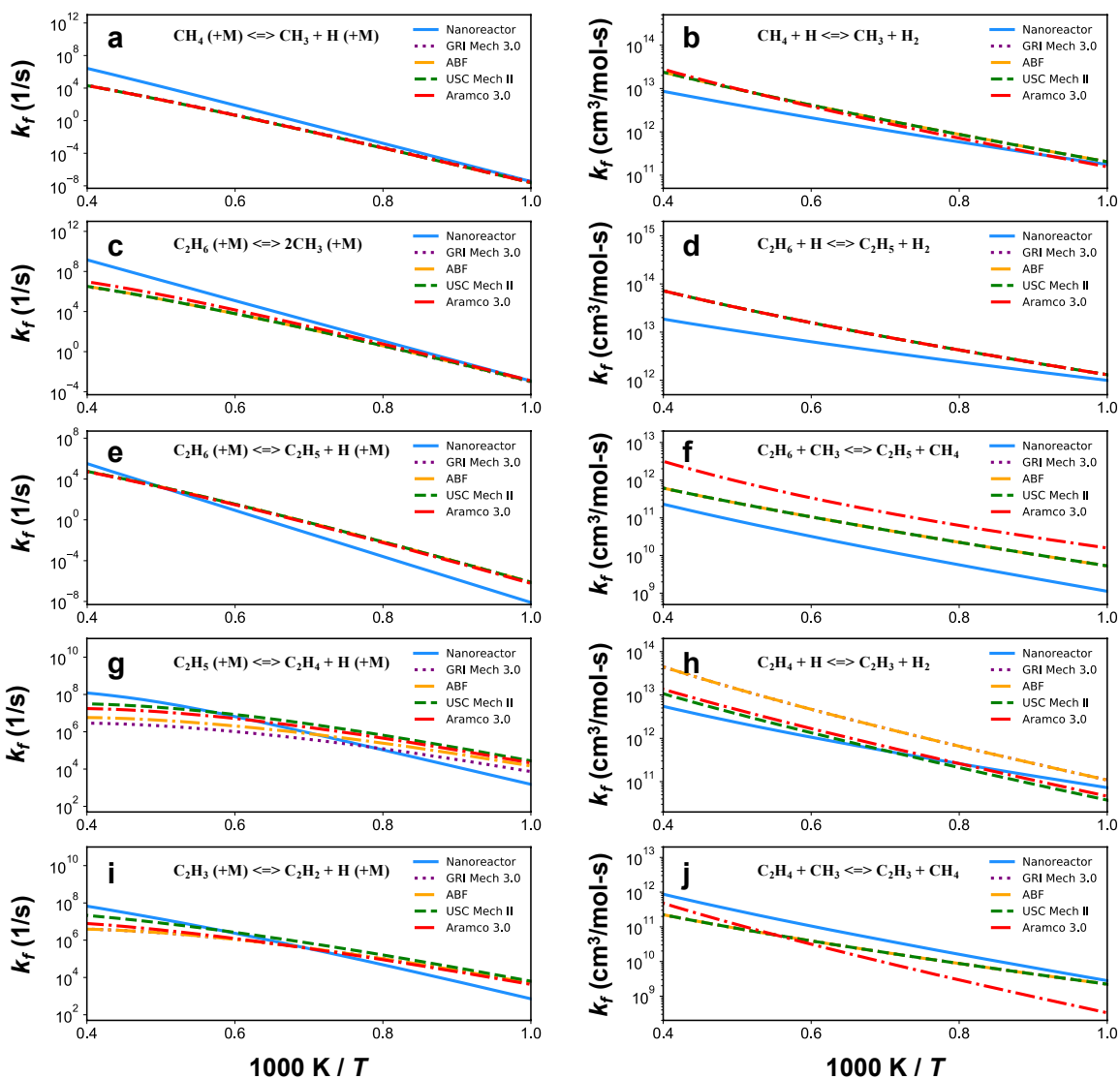


Figure S4. Forward reaction rates of (a) $\text{CH}_4 (+\text{M}) \rightleftharpoons \text{CH}_3 + \text{H} (+\text{M})$, (b) $\text{CH}_4 + \text{H} \rightleftharpoons \text{CH}_3 + \text{H}_2$, (c) $\text{C}_2\text{H}_6 (+\text{M}) \rightleftharpoons 2\text{CH}_3 (+\text{M})$, (d) $\text{C}_2\text{H}_6 + \text{H} \rightleftharpoons \text{C}_2\text{H}_5 + \text{H}_2$, (e) $\text{C}_2\text{H}_6 (+\text{M}) \rightleftharpoons \text{C}_2\text{H}_5 + \text{H} (+\text{M})$, (f) $\text{C}_2\text{H}_6 + \text{CH}_3 \rightleftharpoons \text{C}_2\text{H}_5 + \text{CH}_4$, (g) $\text{C}_2\text{H}_5 (+\text{M}) \rightleftharpoons \text{C}_2\text{H}_4 + \text{H} (+\text{M})$, (h) $\text{C}_2\text{H}_4 + \text{H} \rightleftharpoons \text{C}_2\text{H}_3 + \text{H}_2$, (i) $\text{C}_2\text{H}_3 (+\text{M}) \rightleftharpoons \text{C}_2\text{H}_2 + \text{H} (+\text{M})$, and (j) $\text{C}_2\text{H}_4 + \text{CH}_3 \rightleftharpoons \text{C}_2\text{H}_3 + \text{CH}_4$ computed by the nanoreactor, USC Mech II,² ABF,³ GRI Mech 3.0,⁴ and AramcoMech 3.0⁵ kinetic models at 1 atm pressure and 1000 – 2500 K. Reactions in the left column (a, c, e, g, i) are unimolecular and have pressure-dependent rates; those in the right column (b, d, f, h, j) are bimolecular and have pressure-independent rates.

Table S6. Reaction rates calculated from the nanoreactor (NR), GRI Mech 3.0 (GRI),² ABF,³ USC Mech II (USC),⁴ and AramcoMech 3.0 (AM).⁵

Rxn. index ^a	Rate Coefficient k_f ^b									
	$T = 1000 \text{ K}$					$T = 2000 \text{ K}$				
	NR	GRI	ABF	USC	AM	NR	GRI	ABF	USC	AM
Unimolecular Reactions										
a	3.38×10^{-8}	3.14×10^{-8}	2.43×10^{-8}	2.43×10^{-8}	2.49×10^{-8}	1.56×10^4	4.03×10^2	3.61×10^2	3.61×10^2	3.63×10^2
c	7.64×10^{-2}	9.47×10^{-4}	1.10×10^{-3}	1.10×10^{-3}	1.27×10^{-3}	1.30×10^7	1.79×10^5	1.71×10^5	1.71×10^5	4.75×10^5
e	7.88×10^{-9}	7.63×10^{-7}	7.63×10^{-7}	7.63×10^{-7}	5.87×10^{-7}	1.62×10^3	1.66×10^3	1.66×10^3	1.66×10^3	1.50×10^3
g	1.52×10^3	7.34×10^3	1.47×10^4	2.77×10^4	2.13×10^4	1.52×10^7	2.07×10^6	4.14×10^6	2.01×10^7	1.17×10^7
i	7.18×10^2	5.09×10^3	5.09×10^3	6.35×10^3	4.25×10^3	1.37×10^7	2.51×10^6	2.51×10^6	8.39×10^6	3.56×10^6
Bimolecular Reactions										
b	1.76×10^{11}	2.04×10^{11}	2.04×10^{11}	2.04×10^{11}	1.56×10^{11}	4.18×10^{12}	9.61×10^{12}	9.61×10^{12}	9.61×10^{12}	9.84×10^{12}
d	9.96×10^{11}	1.30×10^{12}	1.30×10^{12}	1.30×10^{12}	1.30×10^{12}	1.06×10^{13}	3.23×10^{13}	3.23×10^{13}	3.23×10^{13}	3.23×10^{13}
f	1.13×10^9	5.30×10^9	5.30×10^9	5.30×10^9	1.58×10^{10}	8.26×10^{10}	2.46×10^{11}	2.46×10^{11}	2.46×10^{11}	9.38×10^{11}
h	7.27×10^{10}	1.09×10^{11}	1.09×10^{11}	3.76×10^{10}	4.62×10^{10}	2.31×10^{12}	1.37×10^{13}	1.37×10^{13}	3.65×10^{12}	4.58×10^{12}
j	2.80×10^9	2.22×10^9	2.22×10^9	2.22×10^9	3.31×10^8	2.90×10^{11}	8.97×10^{10}	8.97×10^{10}	8.97×10^{10}	1.15×10^{11}

^a The reaction (Rxn.) index is referred to the reactions in the corresponding panels of **Fig. S4**.

^b Rate coefficients k_f are calculated at $P = 1 \text{ atm}$. The units for k_f is s^{-1} for unimolecular dissociation reactions a, c, e, g, i, and $\text{cm}^3 \text{mol}^{-1} \text{s}^{-1}$ for bimolecular reactions b, d, f, h, j.

Section S7. Additional Details in Kinetic Modeling.

In the main text, we presented kinetic modeling results in **Figure 3** and **Figure 6**. The simulated species mole fractions are validated against experimental data collected from two shock tube (ST) facilities²⁰ and a flow reactor (FR) facility,²¹ respectively. Simulations are performed as initial value problems in 0D homogeneous reactor module in Cantera¹ with initial temperatures and pressures specified. Simulated species mole fractions are taken at the end of the simulation (corresponding to the total reaction time t_{rec}). Each solid line in **Figures 3** and **6** is constructed with a series of simulations with initial temperatures set in a predefined range and a reasonably small temperature increment. **Table S7** lists the initial conditions (P_0 , range of T_0 , and initial species mole fractions), simulated reaction time t_{rec} , and simulation assumptions. Taking Expt. No.1. as an example, a series of 0D homogeneous reactor simulations is conducted with initial temperature T_0 ranging from 1300 to 2400 K and a 25 K step size. P_0 and t_{rec} are kept identical in each simulation. The blue solid line in **Figure 3a** is constructed by connecting the nanoreactor-kinetic-model-simulated CH₄ mole fractions taken at the end of each simulation (i.e., at $t_{\text{rec}} = 2.87$ ms). The same procedure is used to construct the simulation lines for other kinetic models.

Table S7. Simulation initial conditions, reaction times (t_{rec}), and assumptions.

Expt. No.	Facility	P_0 (bar/atm)	T_0 (K)	Initial species mole fractions	t_{rec} (ms)	Assumption ^b
1	ST ²⁰	1.4 bar	1300 – 2400	10% CH ₄ /Ar	2.87	Adiabatic, constant volume, 0D homogeneous reactor
2	ST ²⁰	30.0 bar	1100 – 2000	10% CH ₄ /Ar	14.76	Adiabatic, constant volume, 0D homogeneous reactor
3	FR ²¹	1.0 atm	1050 – 1500	10% CH ₄ /N ₂	$4.55 \times 10^6 / T_0(\text{K})^a$	Constant pressure, constant temperature, 0D homogeneous reactor

^a The simulation time in the flow reactor is taken from the experiment gas residence time. Given the simulation temperature range of 1050 – 1500 K, the simulated reaction t_{rec} is in the range of 3033 – 4333 ms.

^b The simulation assumption is generally adopted from both the corresponding experiments and past literatures. Kinetic modeling of shock tube experiments is generally performed as an initial value problem in an adiabatic, 0D homogeneous reactor with either constant volume or constant pressure assumption. We choose constant volume assumption according to the experiment paper. Experiments in the flow reactor are usually conducted with heating to maintain a constant temperature environment. The pressure is also held to be constant during the experiment.

For each experimental data point collected, the experimental initial pressure and reaction time may vary. **Table S8** shows the actual experimental pressure (P_0), temperature (T_0), and reaction time t_{rec} for each experimental data point in the two ST experiments. For the convenience of simulation and visualization, we conducted simulations of the two ST experiments with P_0 and t_{res} being the average of the actual values for each data point (e.g., $P_0 = 1.4$ bar for Expt. No. 1 in

Table S7 corresponds to the average value of the second column in **Table S8**). With this consistency, we can conveniently present the simulated species mole fractions as a function of temperature only, and these results are shown as continuous lines in **Figures 3** and **6**. A follow-up question is, how much would the results from simulations taking average P_0 and t_{rec} differ from the direct simulation results with the actual P_0 and t_{rec} for each experimental data point? The comparison between two simulation approaches is shown in **Figure S5**. We simulated the CH₄ mole fractions of Expt. No. 1 (left panel) and Expt. No. 2 (right panel). The lines correspond to the results with average- P_0/t_{rec} simulation approach (which are exactly the lines in **Figure 3a** and **3b**), and the open circles correspond to the results with actual- P_0/t_{rec} simulation method. As can be seen, the difference induced by the two simulation methods are negligible. For the flow reactor experiment (Expt. No. 3), we carried out simulations with t_{rec} varying as a function of temperature (i.e., $t_{\text{rec}} = 4.55 \times 10^6 / T(\text{K})$ ms, which is reported in the original paper) and constant pressure P_0 of 1 atm, due to the lack of information of each actual P_0 in the original paper.

Table S8. Actual temperatures, pressures, and reaction times in the shock tube experiments. Data are taken from the original experiment paper.²⁰

Expt. No. 1			Expt. No. 2		
T_0 (K)	P_0 (bar)	t_{rec} (ms)	T_0 (K)	P_0 (bar)	t_{rec} (ms)
1635	1.68	2.6	1347	27.8	16.79
1694	1.66	2.6	1390	29.6	15.47
1720	1.54	2.4	1439	27.8	18.13
1745	1.35	2.6	1513	30.5	15.53
1815	1.58	2.5	1665	32.3	13.62
1935	1.44	2.4	1758	31.9	13.84
2021	1.38	2.5	1792	29.7	13.35
2131	1.32	2.8	1916	30.5	13.20
2234	1.22	3.7	1973	29.3	12.90
2355	1.11	3.6			
2400	0.91	3.9			

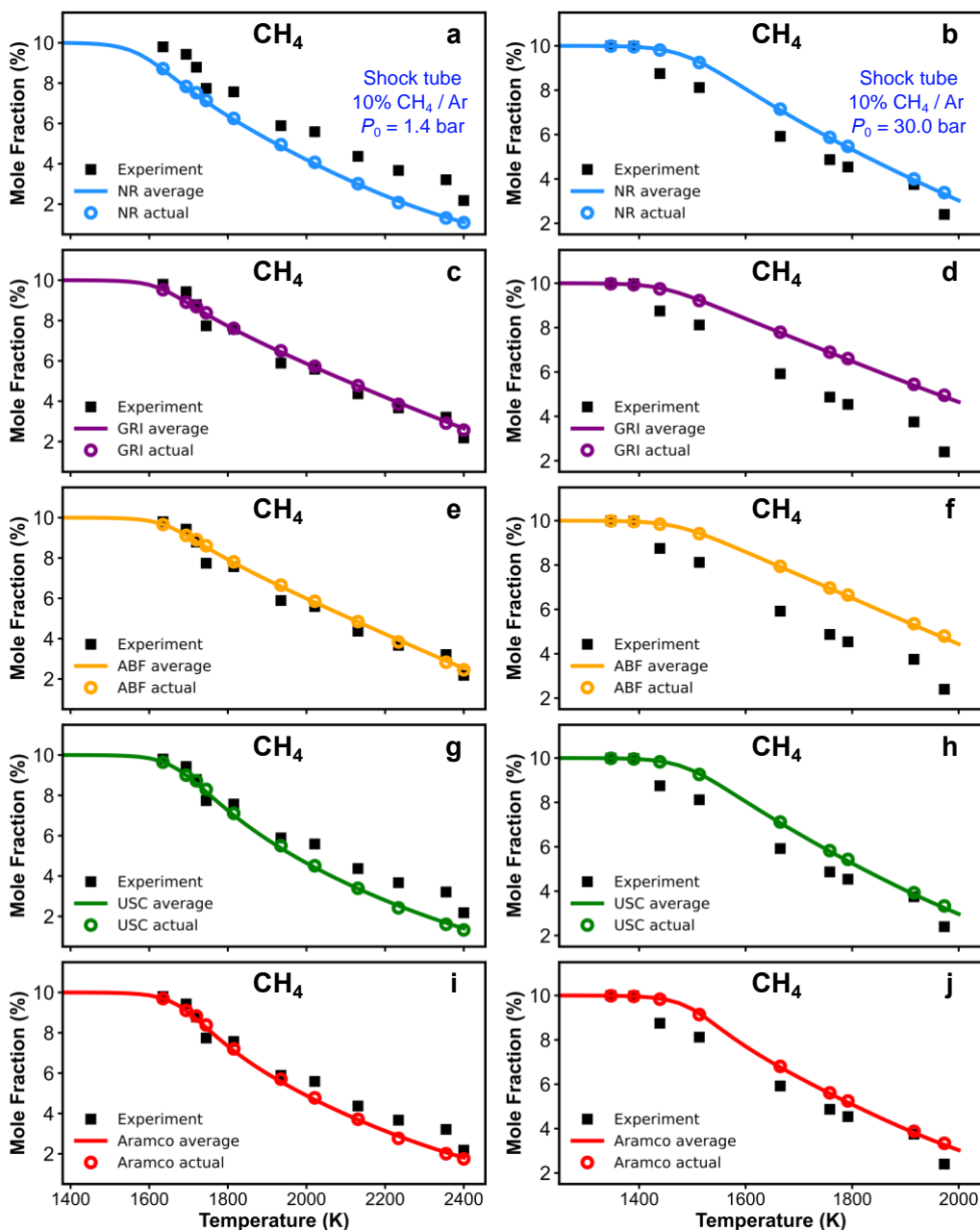


Figure S5. Comparisons of simulated CH₄ concentrations between using the average P_0 & t_{rec} (same results from **Figure 3**) and the actual P_0 & t_{rec} taken from the shock tube experimental data.²⁰ The experimental/simulation condition of the left column (a, c, e, g, & i) corresponds to the same condition of **Figure 3a**: 10% CH₄ / Ar, $P_0 = 1.4$ bar, and $t_{rec} = 2.87$ ms; the condition of the right column (b, d, f, h, & j) corresponds to the same condition of **Figure 3b**: 10% CH₄ / Ar, $P_0 = 30$ bar, and $t_{rec} = 14.8$ ms. Simulations are performed using (a & b) the nanoreactor (NR), (c & d) GRI Mech 3.0 (GRI), (e & f) ABF, (g & h) USC Mech II (USC), and (i & j) AramcoMech 3.0 (Aramco) model, respectively. Solid square symbols: experimental data, solid lines: simulation results using the average P_0 & t_{rec} , open circle symbols: simulation results using the actual P_0 & t_{rec} .

Section S8. Examples of “Rare Events” During Reaction Discovery Runs.

In **Section 3.1**, we mentioned the nanoreactor not only discovers almost all the key reactions impacting methane pyrolysis chemistry, but also uncovers several reactions which are not considered by any literature kinetic models used in this work. We take two examples here: $\text{CH}_4 + \text{CH}_3 \rightleftharpoons \text{C}_2\text{H}_6 + \text{H}$ and $\text{C}_2\text{H}_6 + \text{H}_2 \rightleftharpoons \text{C}_2\text{H}_4 + 2\text{H}_2$. **Figure S6** shows their optimized reaction paths using the growing string method (GSM).^{22,23} The barrier for reaction $\text{CH}_4 + \text{CH}_3 \rightleftharpoons \text{C}_2\text{H}_6 + \text{H}$ is found to be 62 kcal/mol (45 kcal/mol for the reverse reaction), and 78 kcal/mol (37 kcal/mol reverse) for reaction $\text{C}_2\text{H}_6 + \text{H}_2 \rightleftharpoons \text{C}_2\text{H}_4 + 2\text{H}_2$, both of which are high. Furthermore, from the sensitivity analysis results in **Figure 5**, neither reaction shows up in the top-ten ranked reactions impacting CH_4 , which is probably due to their high reaction barriers. This suggests that the probability for either of these reactions to occur during normal CH_4 combustion conditions is quite low, and they are triggered by the piston compression forces in the nanoreactor. **Table S9** lists the optimized transition state configurations taking the initial guess from the highest-energy-geometry in the optimized reaction path (**Figure S6**), along with their frequencies. Only one imaginary frequency is found for each of the transition state configurations. Confirmation of whether these two reactions are elementary probably requires further work such as intrinsic reaction coordinate (IRC) calculations. Nevertheless, these examples perfectly demonstrate the nanoreactor’s potential to discover rare reaction events.

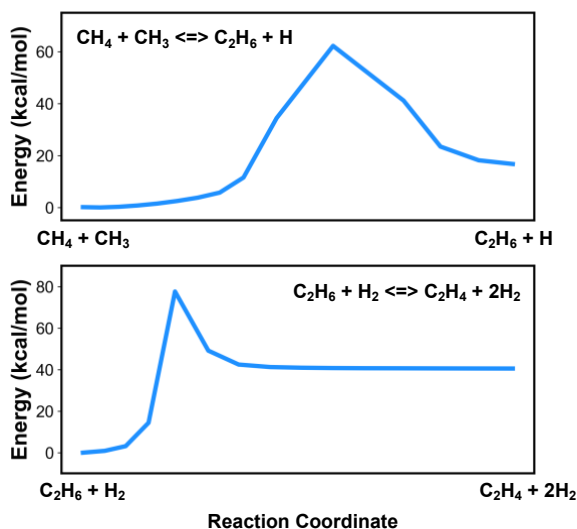
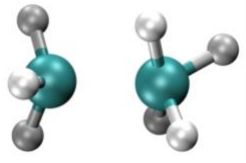
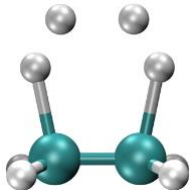


Figure S6. Optimized reaction paths for $\text{CH}_4 + \text{CH}_3 \rightleftharpoons \text{C}_2\text{H}_6 + \text{H}$ (top panel) and $\text{C}_2\text{H}_6 + \text{H}_2 \rightleftharpoons \text{C}_2\text{H}_4 + 2\text{H}_2$ (bottom panel). In each optimized path, the geometry of the highest-energy point is taken for a transition state optimization. Details of the optimized transition state structures are included in **Table S9**.

Table S9. Optimized transition state (TS) geometries and their frequencies

Reaction	Optimized TS geometries	TS frequencies (cm ⁻¹)
$\text{CH}_4 + \text{CH}_3 \rightleftharpoons \text{C}_2\text{H}_6 + \text{H}$		-1009.8 , 182.2, 311.8, 651.4, 812.5, 921.3, 1152.8, 1162.9, 1292.9, 1389.6, 1404.6, 1472.8, 1485.3, 1499.8, 1775.6, 1868.3, 2560.7, 3037.3, 3114.3, 3152.6, 3178.3
$\text{C}_2\text{H}_6 + \text{H}_2 \rightleftharpoons \text{C}_2\text{H}_4 + 2\text{H}_2$		-1657.6 , 456.6, 603.6, 618.1, 847.7, 907.0, 1025.0, 1037.6, 1048.0, 1199.5, 1208.0, 1212.5, 1226.2, 1279.3, 1290.8, 1334.4, 1476.0, 1562.7, 2141.8, 2704.0, 3141.6, 3151.3, 3219.1, 3240.0

Section S9. Discussion on Chemically Activated Reaction $2\text{CH}_3 \rightleftharpoons \text{C}_2\text{H}_5 + \text{H}$.

Figures 4 and 5 in the main text show sensitivity analysis results of CH_4 mole fraction with respect to reaction rates. The results indicate the nanoreactor kinetic model does not show the expected impact of reaction $2\text{CH}_3 \rightleftharpoons \text{C}_2\text{H}_5 + \text{H}$. In this section, we discuss the results for this reaction. Historically, this reaction has been thought to be chemically activated. Under high-temperature reaction conditions, the recombination of two methyl (CH_3) radicals forms a vibrationally activated adduct (C_2H_6^*) which is so energetic that it can skip over the ethane (C_2H_6) potential energy well and directly form the product of ethyl (C_2H_5) and hydrogen (H) radicals. This well-skipping phenomenon can also happen in the reverse reaction direction.

During the discovery phase in the nanoreactor workflow, reaction $2\text{CH}_3 \rightleftharpoons \text{C}_2\text{H}_5 + \text{H}$ has been found. The reaction path is further optimized by the growing string method (GSM),^{22,23} and the result is shown in **Figure S7**. As seen, the GSM-optimized path contains a peak instead of the deep potential energy well of C_2H_6 molecule. This is because the path optimization is performed on a potential energy surface with triplet spin multiplicity. The reaction barrier is 61 kcal/mol (47 kcal/mol for the reverse reaction). Transition state optimization calculation is further performed taking the geometry of the highest-energy-point in **Figure S7**, and the results are summarized in **Table S10**. Two imaginary frequencies are found, with one having large frequency which may correspond to the normal mode along the reaction coordinate, and another having a relatively small frequency. This suggests that the optimized configuration lies close to a first-order saddle point.

Taking the above information, the rate coefficient of $2\text{CH}_3 \rightleftharpoons \text{C}_2\text{H}_5 + \text{H}$ in the nanoreactor kinetic model can be calculated and compared with the values in literature kinetic models. The comparison is illustrated in **Figure S8**. Clearly the rate coefficient in the NR model appears to be much lower than the rates in all four literature models, where the theoretical RRKM¹⁷⁻¹⁹ rate parameters from Stewart et al²⁴ are adopted. Furthermore, a small sensitivity test is also conducted by replacing the rate of $2\text{CH}_3 \rightleftharpoons \text{C}_2\text{H}_5 + \text{H}$ in the nanoreactor by the rate of Stewart et al,²⁴ and the results is shown in **Figure S9**. Overall, the results are not very sensitive to the value of this rate coefficient. However, the impact is noticeable for C_2H_4 (**Figure S9c**).

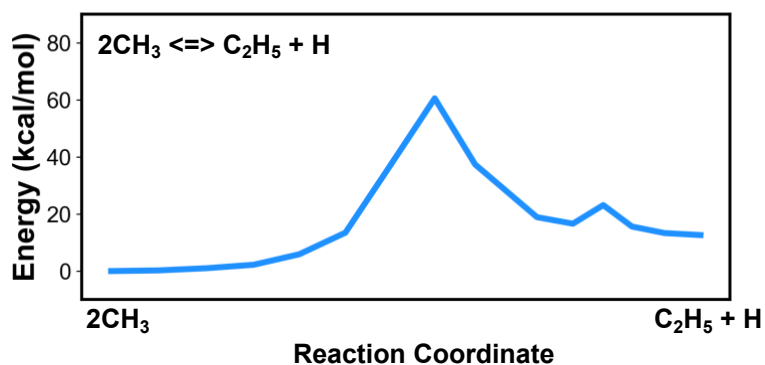
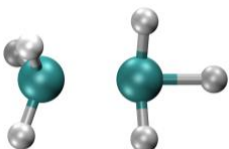


Figure S7. Optimized reaction paths for $2\text{CH}_3 \rightleftharpoons \text{C}_2\text{H}_5 + \text{H}$ on the triplet spin surface. The geometry of the highest-energy point is taken for a transition state optimization. Details of the optimized transition state configuration are included in **Table S9**.

Table S10. Optimized transition state (TS) geometry and its frequencies for the triplet spin surface.

Reaction	Optimized TS geometry	TS frequencies (cm^{-1})
$2\text{CH}_3 \rightleftharpoons \text{C}_2\text{H}_5 + \text{H}$		-1485.4, -95.8 , 233.7, 606.3, 640.2, 685.9, 887.7, 985.4, 1219.7, 1420.7, 1461.7, 1473.3, 1478.0, 2876.8, 3043.3, 3155.8, 3165.0, 3178.4

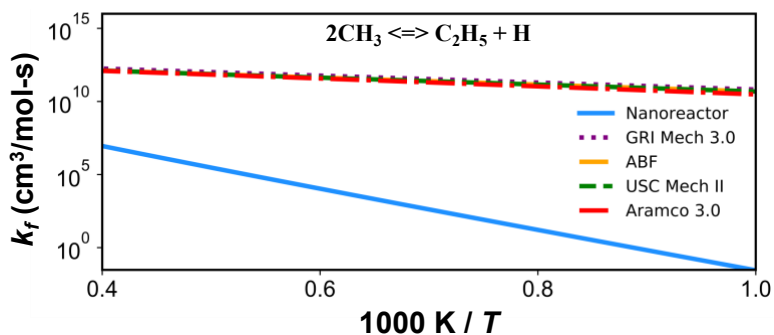


Figure S8. Forward reaction rate of $2\text{CH}_3 \rightleftharpoons \text{C}_2\text{H}_5 + \text{H}$ computed by the nanoreactor, USC Mech II,² ABF,³ GRI Mech 3.0,⁴ and AramcoMech 3.0⁵ kinetic models at 1 atm pressure and 1000 – 2500 K temperature range.

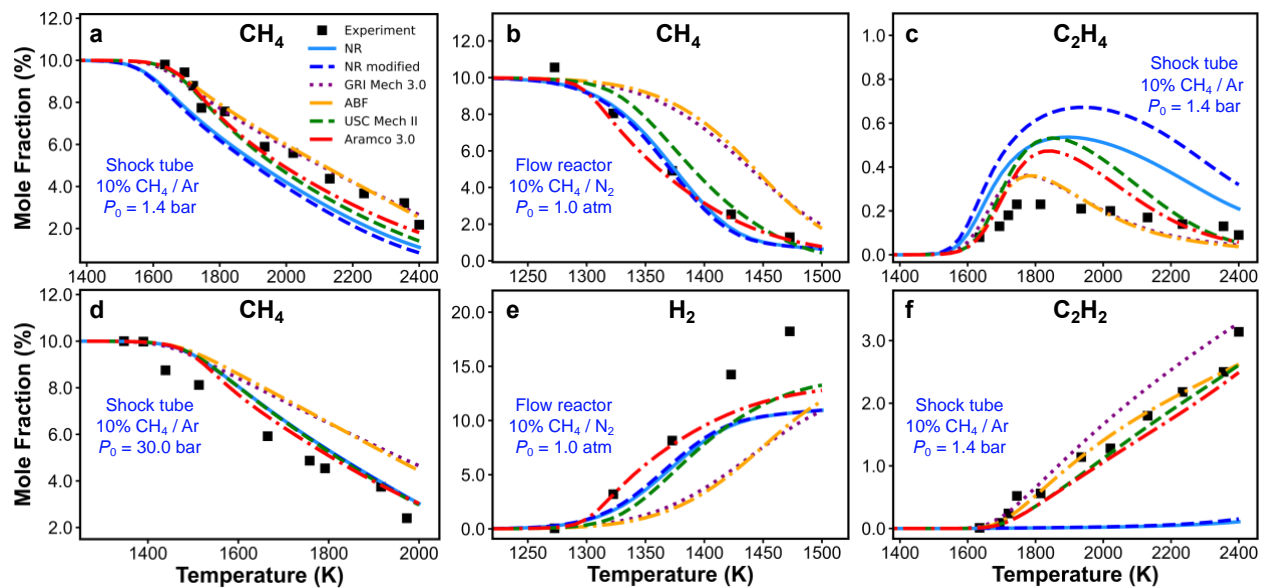


Figure S9. Validation plots with the modified NR kinetic model replacing the $2\text{CH}_3 \leftrightarrow \text{C}_2\text{H}_5 + \text{H}$ rate by that from GRI Mech 3.0. Simulation conditions: (a) (c) & (f) 10% CH_4 / Ar , $P_0 = 1.4$ bar, and $t_{\text{rec}} = 2.87$ ms; (b) 10% CH_4 / Ar , $P_0 = 30$ bar, and $t_{\text{rec}} = 14.8$ ms; (c) & (d) 10% CH_4 / N_2 , $P_0 = 1.0$ atm, and t_{rec} is reported in the experimental paper²⁰ as a function of the initial temperature, as $t_{\text{rec}} = 4.55 \times 10^6 / T_0(\text{K})$ ms.

Section S10. Additional Results from the Sensitivity Analysis.

This section includes additional results from both the local brute-force sensitivity analysis and the Monte Carlo sensitivity analysis. Specifically, **Figures S10-S13** show the sensitivity bar spectra of CH₄ concentration computed for the conditions: 10% CH₄ / Ar, $P_0 = 1.4$ bar, $t_{\text{rec}} = 2.87$ ms, and $T_0 = 1800, 2000, 2200,$ and 2400 K, respectively. **Figure S14** shows the Monte Carlo sensitivity scatter plots of CH₄ concentrations simulated for the conditions: 10% CH₄ / Ar, $P_0 = 30$ bar, and $t_{\text{rec}} = 14.8$ ms (same as **Figure 3b**). **Figure S15** presents the MC plots of CH₄ (**a, c,** and **e**) and H₂ (**b, d,** and **f**) concentrations simulated for conditions: 10% CH₄ / N₂, $P_0 = 1.0$ atm, and $t_{\text{rec}} = 4.55 \times 10^6 / T_0(\text{K})$ ms (same as **Figures 3c** and **3d**).

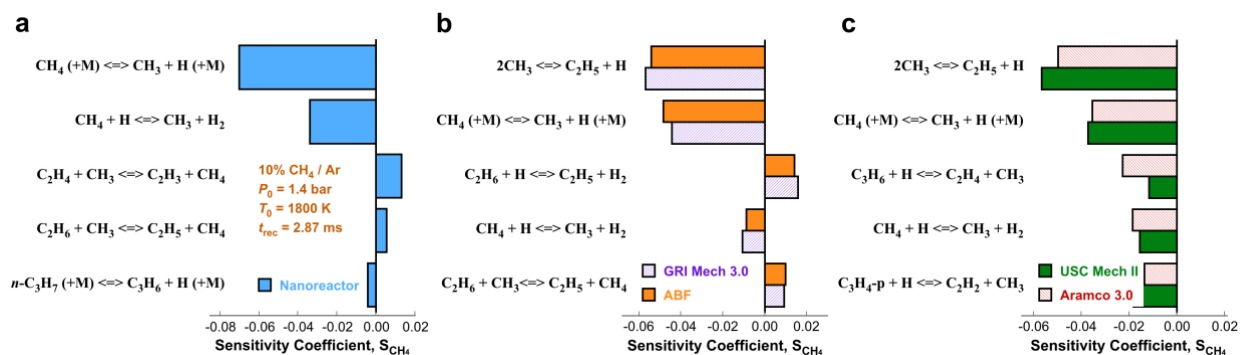


Figure S10. Sensitivity bar spectra of CH₄ concentration computed under condition 10% CH₄ / Ar, $P_0 = 1.4$ bar, $T_0 = 1800$ K, and $t_{\text{rec}} = 2.87$ ms. Five reaction kinetic models are analyzed, including (a) the nanoreactor, (b) GRI Mech 3.0² & ABF,³ (c) USC Mech II⁴ & Aramco 3.0.⁵

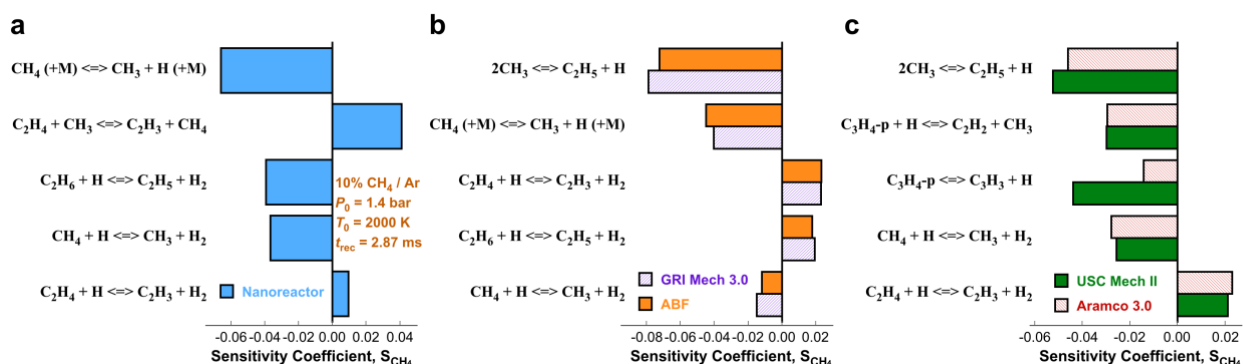


Figure S11. Sensitivity bar spectra of CH₄ concentration computed under condition 10% CH₄ / Ar, $P_0 = 1.4$ bar, $T_0 = 2000$ K, and $t_{\text{rec}} = 2.87$ ms. Five reaction kinetic models are analyzed, including (a) the nanoreactor, (b) GRI Mech 3.0² & ABF,³ (c) USC Mech II⁴ & Aramco 3.0.⁵

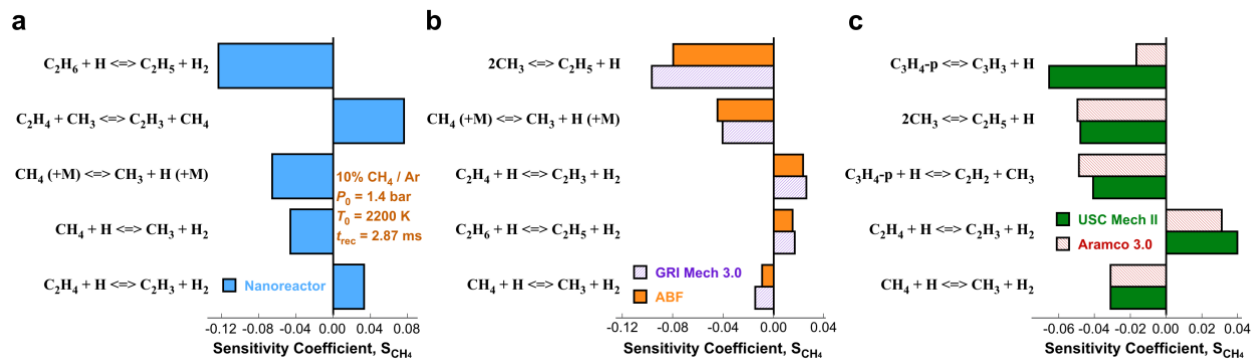


Figure S12. Sensitivity bar spectra of CH_4 concentration computed under condition 10% CH_4 / Ar , $P_0 = 1.4$ bar, $T_0 = 2200$ K, and $t_{\text{rec}} = 2.87$ ms. Five reaction kinetic models are analyzed, including (a) the nanoreactor, (b) GRI Mech 3.0² & ABF,³ (c) USC Mech II⁴ & Aramco 3.0.⁵

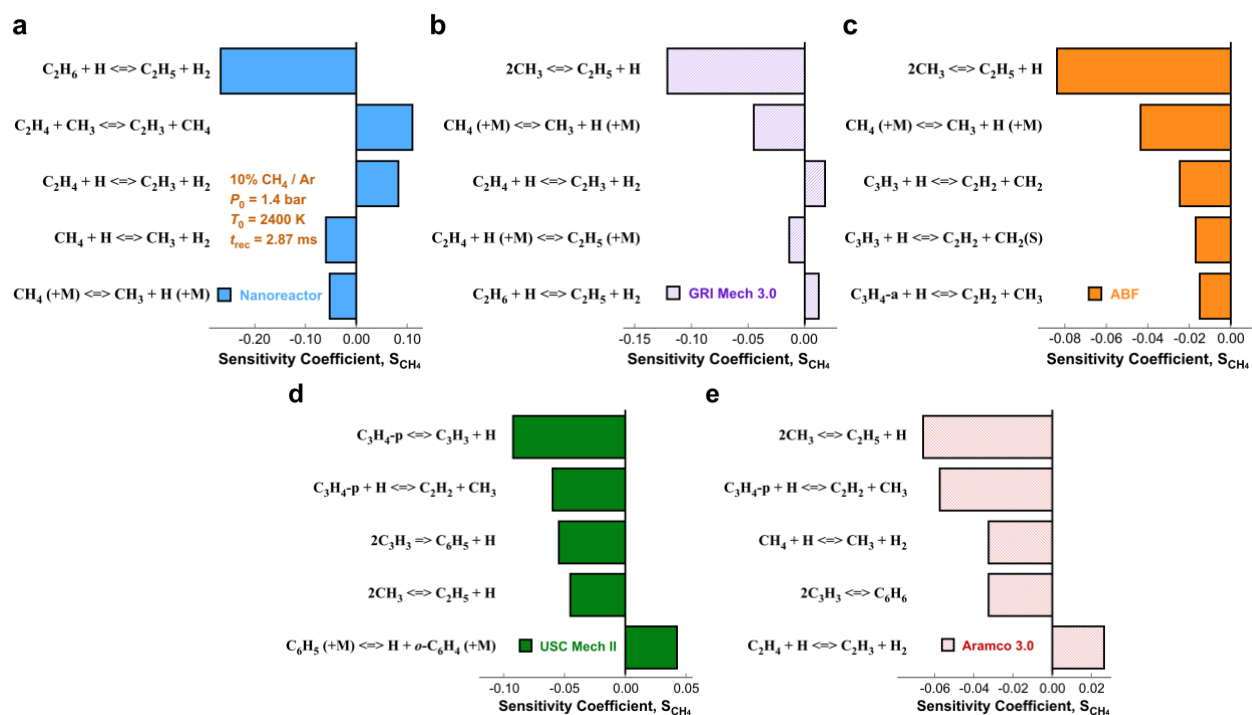


Figure S13. Sensitivity bar spectra of CH_4 concentration computed under condition 10% CH_4 / Ar , $P_0 = 1.4$ bar, $T_0 = 2400$ K, and $t_{\text{rec}} = 2.87$ ms. Five reaction kinetic models are analyzed, including (a) the nanoreactor, (b) GRI Mech 3.0,² (c) ABF,³ (d) USC Mech II,⁴ and (e) Aramco 3.0.⁵

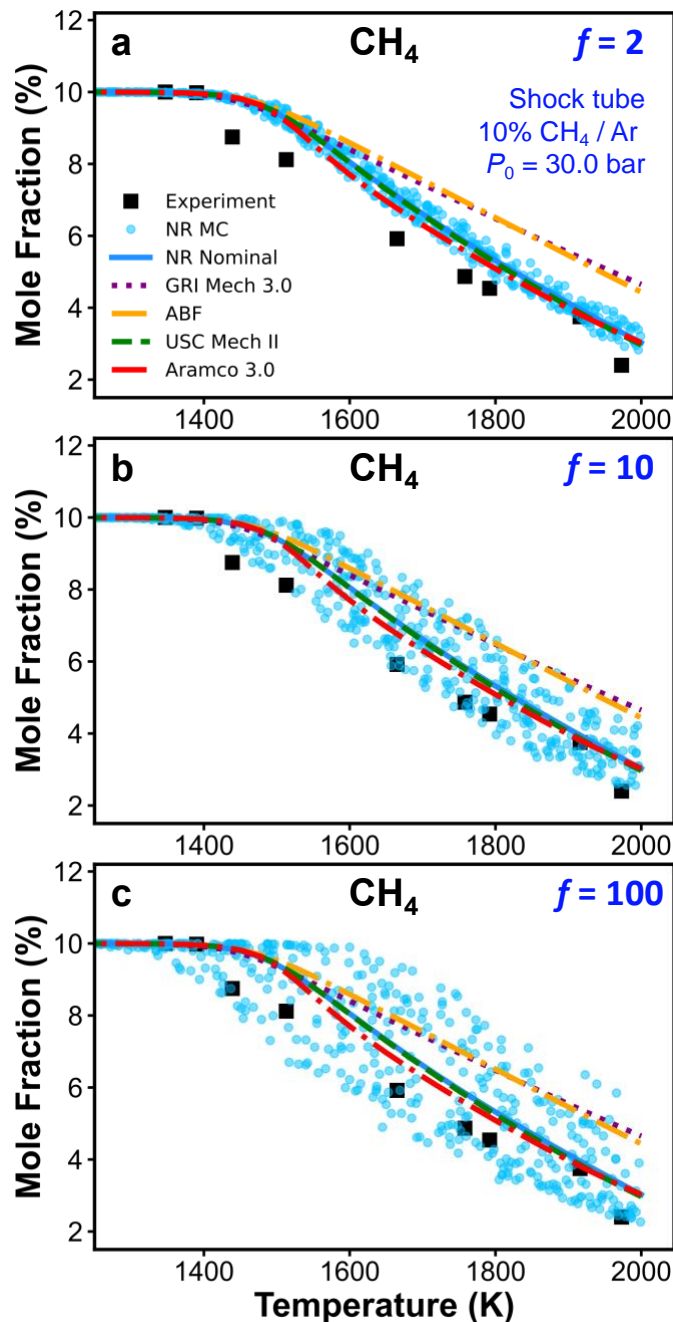


Figure S14. Monte Carlo (MC) sensitivity scatter plots of CH_4 concentrations simulated by the nanoreactor (NR) reaction model along with experimental data and simulations obtained from other literature kinetic models. Each filled circle represents a simulation using one MC sample of NR model in which each rate constant is perturbed within an upper-limit factor of $f = 2$ (a), 10 (b), and 100 (c), respectively from the nominal values, assuming a uniform distribution in the log space of the rate coefficient. The sensitivity analyses are performed under condition 10% CH_4 / Ar , $P_0 = 30$ bar, and $t_{\text{rec}} = 14.8$ ms.

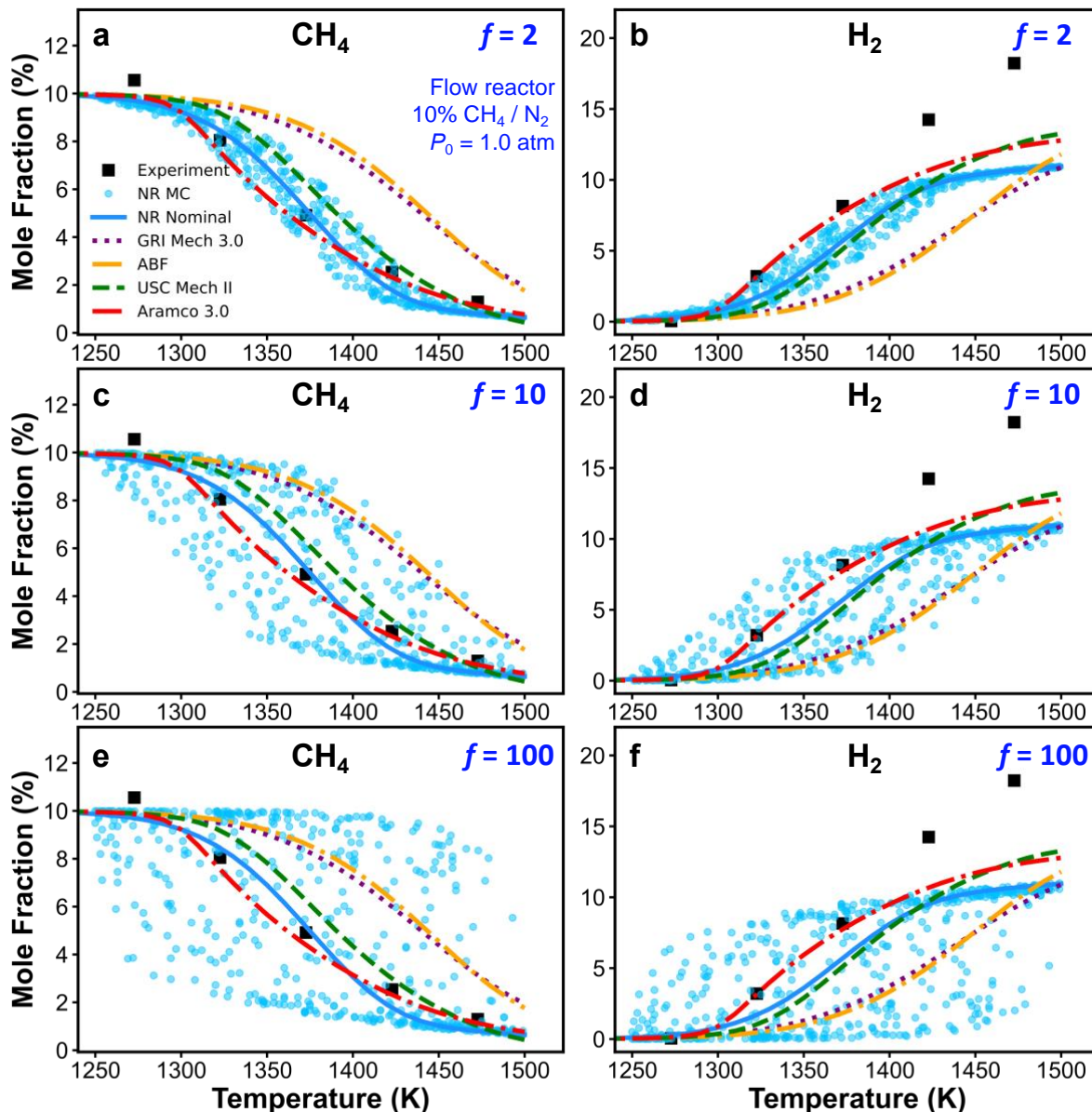


Figure S15. Monte Carlo (MC) sensitivity scatter plots of CH₄ (a, c, and e) and H₂ (b, d, and f) concentrations simulated by the nanoreactor (NR) reaction model along with experimental data and simulations obtained from other literature kinetic models. Each filled circle represents a simulation using one MC sample of NR model in which each rate constant is perturbed within an upper-limit factor of 2 (a, & b), 10 (c & d), and 100 (e & f), respectively from the nominal values, assuming a uniform distribution in the log space of the rate coefficient. The sensitivity analyses are performed under condition 10% CH₄ / N₂, $P_0 = 1.0$ atm, and t_{rec} is reported in the experimental paper²⁰ as a function of the initial temperature, as $t_{\text{rec}} = 4.55 \times 10^6 / T_0(\text{K})$ ms.

References

1. D. G. Goodwin, H. K. Moffat, I. Schoegl, R. L. Speth, and B. W. Weber, Cantera: An object-oriented software toolkit for chemical kinetics, thermodynamics, and transport processes. <https://www.cantera.org>, 2022. Version 2.6.0. doi:10.5281/zenodo.6387882.
2. G. P. Smith, D. M. Golden, M. Frenklach, N. W. Moriatry, E. Boris, G. Mikhail, C. T. Bowman, R. K. Hanson, S. Song, W. C. Gardiner, V. V. Lissianski, and Z. Qin, GRI-Mech 3.0. <http://combustion.berkeley.edu/gri-mech/version30/text30.html>, accessed March 1, 2023.
3. J. Appel, H. Bockhorn, and M. Frenklach, Kinetic modeling of soot formation with detailed chemistry and physics: laminar premixed flames of C₂ hydrocarbons. *Combust. Flame* **121**, 122-136 (2000).
4. H. Wang, X. You, A. V. Joshi, S. G. Davis, A. Laskin, F. Egolfopoulos, and C. K. Law, USC Mech Version II. High-temperature combustion reaction model of H₂/CO/C₁-C₄ compounds. https://ignis.usc.edu:80/Mechanisms/USC-Mech%20II/USC_Mech%20II.htm, accessed July 1, 2022.
5. C.-W. Zhou, Y. Li, U. Burke, C. Banyon, K. P. Somers, S. Ding, S. Khan, J. W. Hargis, T. Sikes, O. Mathieu, E. L. Peterson, M. AlAbbad, A. Farooq, Y. Pan, Y. Zhang, Z. Huang, J. Lopez, Z. Loparo, S. S. Vasu, and H. J. Curran, An experimental and chemical kinetic modeling study of 1, 3-butadiene combustion: Ignition delay time and laminar flame speed measurements. *Combust. Flame* **197**, 423-438 (2018).
6. R. S. Mulliken, Electronic population analysis on LCAO–MO molecular wave functions. I. *J. Chem. Phys.* **23**, 1833-1840 (1955).
7. D. A. McQuarrie, *Statistical Mechanics*. Harper & Row, New York, 1976.
8. S. Grimme, Supramolecular binding thermodynamics by dispersion-corrected density functional theory. *Chem. Eur. J.* **18**, 9955-9964 (2012).
9. J.-D. Chai and M. Head-Gordon, Long-range corrected hybrid density functionals with damped atom–atom dispersion corrections. *Phys. Chem. Chem. Phys.* **10**, 6615-6620 (2008).
10. K. Yamaguchi, F. Jensen, A. Dorigo, and K. Houk, A spin correction procedure for unrestricted Hartree-Fock and Møller-Plesset wavefunctions for singlet diradicals and polyradicals. *Chem. Phys. Lett.* **149**, 537-542 (1988).
11. Y. Kitagawa, T. Saito, and K. Yamaguchi, Approximate spin projection for broken-symmetry method and its application. *Symmetry (Group Theory) and Mathematical Treatment in Chemistry* 2018, 121-139.
12. B. J. McBride, NASA Glenn coefficients for calculating thermodynamic properties of individual species. National Aeronautics and Space Administration, John H. Glenn Research Center 2002.
13. E. Wigner, The transition state method. *Trans. Faraday Soc.* **34**, 29-41 (1938).
14. H. Eyring, The activated complex in chemical reactions. *J. Chem. Phys.* **3**, 107-115 (1935).
15. M. G. Evans and M. Polanyi, Some applications of the transition state method to the calculation of reaction velocities, especially in solution. *Trans. Faraday Soc.* **31**, 875-894 (1935).

16. C. N. Hinshelwood, On the theory of unimolecular reactions. *Proc. Roy. Soc. A* **113**, 230-233 (1926).
17. O. K. Rice and H. C. Ramsperger, Theories of unimolecular gas reactions at low pressures. *J. Am. Chem. Soc.* **49**, 1617-1629 (1927).
18. L. S. Kassel, Studies in homogeneous gas reactions. I. *J. Phys. Chem.* **32**, 225-242 (1928).
19. R. A. Marcus, Unimolecular dissociations and free radical recombination reactions. *J. Chem. Phys.* **20**, 359-364 (1952).
20. D. Nativel, B. Shu, J. Herzler, M. Fikri, and C. Schulz, Shock-tube study of methane pyrolysis in the context of energy-storage processes. *Proc. Combust. Inst.* **37**, 197-204 (2019).
21. C. Keramiotis, G. Vourliotakis, G. Skevis, M. Founti, C. Esarte, N. Sanchez, A. Millera, R. Bilbao, and M. Alzueta, Experimental and computational study of methane mixtures pyrolysis in a flow reactor under atmospheric pressure. *Energy* **43**, 103-110 (2012).
22. P. M. Zimmerman, Growing string method with interpolation and optimization in internal coordinates: Method and examples. *J. Chem. Phys.* **138**, 184102 (2013).
23. P. M. Zimmerman, Reliable transition state searches integrated with the growing string method. *J. Chem. Theory Comput.* **9**, 3043-3050 (2013).
24. P. Stewart, C. Larson, and D. Golden, Pressure and temperature dependence of reactions proceeding via a bound complex. 2. Application to $2\text{CH}_3 \rightarrow \text{C}_2\text{H}_5 + \text{H}$. *Combust. Flame* **75**, 25-31 (1989).